College of William and Mary

Williamsburg, Virginia 23185

# New Infrared Detectors and Solar Cells

NASA Grant NSG-1385

Final Report (1 February 1978 - 31 January 1979)

18 April 1979

A. Sher
Principal Investigator

(NASA-CR-158477) NEW INFRARED DETECTORS AND SOLAR CELLS Final Report, 1 Feb. 1978 - 31 Jan. 1979 (College of William and Mary) 75 p HC A04/MF A01 CSCL 10A

N79-21544

Unclas
G3/44 14736

RECEIVED
NASA STI FACILITY
ACCESS DEPT.
MAY 1 '79

Much of the year's accomplishments under this contract are detailed in published papers[1][2][3] and in the two papers included as Appendices A and B of this report. The paper, Appendix A, entitled "$LaF_3$ Insulators for MIS Structures" has been accepted for publication in Applied Physics Letters. The second paper, Appendix B, entitled "Si and GaAs Photocapacitive MIS Infrared Detectors" has been submitted to the Journal of Applied Physics. The abstracts of these papers provide a summary of their content so nothing further will be said about them here.

In addition to the work reported in these papers, several other related projects are nearing completion and will be prepared for publication soon.

1) Fundamental studies of the electronic properties of Si-$SiO_2$, Si-$LaF_3$, GaAs-native oxide, GaAs-$LaF_3$ interface state properties are in progress. The techniques discussed in Appendix A have been used in the Si systems to improve the resolution of interface state densities seen by prior workers, but also the optical methods permit us to assign state types (donor or acceptor) to various features that are observed.

In the GaAs systems we are collecting interface state information of a kind never measured before. The GaAs interface state density is quite unlike the familiar features found in Si. The GaAs case displays a collection of sharp peaks that are well represented as individual quantum levels. The quantum state with the largest population, $\sim 10^{11} cm^{-2}$, at ~0.95 eV from the valence band edge, is the one mostly responsible for pinning the Fermi level in GaAs devices. This pinning tends to prevent GaAs from inverting,

and prevents MOSFET devices constructed from GaAs from working well. It probably is also responsible for establishing the barrier height of Schottky barriers on GaAs. If impurities can be introduced into the interface, e.g., by ion implantation, to move the pinning position and increase the barrier height, then significant improvements in MIS solar cells should result. If, on the other hand, ways can be found to reduce the levels currently there, then MOSFET's can be made to work better.

2) The high speed (<1 MHz) response of the photocapacitive detectors is being investigated. Preliminary results for Si detectors indicate that their detectivities are at least comparable with those of the best PIN devices out to 20 MHz. This study is continuing and we hope to bring it to a conclusion soon.

3) We have recently built and tested a Ge photocapacitive detector. It's peak response is at 1.4 - 1.5 μm. Peak detectivities of $7.5 \times 10^{9}$, $8.7 \times 10^{11}$, and $9.7 \times 10^{12} W^{-1}$-cm-$Hz^{1/2}$ have been observed at temperatures 298, 195 and 77°K respectively. These measurements were made on the first sample we made, so improvements in future generations of devices are expected. However, the $9.7 \times 10^{12} W^{-1}$-cm-$Hz^{1/2}$ detectivity is about an order of magnitude better than any number that we have found on the prior literature.[4]

4) Several methods to use the photocapacitive mechanism in image converters have been invented. Disclosures of these inventions have been submitted to the NASA patent office. Simple tests have been performed which demonstrate that these methods work in principle. However, a thorough

evaluation has not yet been done. We hope to undertake this evaluation in the coming summer.

5) Little has been done on thermal capacitive detectors in this grant period. We plan to emphasize this aspect of the work in the coming months.

6) The work on solar cells has not progressed much in the past grant period. Once again, we hope to undertake definitive experiments to test these devices this summer.

## References

1) A. Sher, R. K. Crouch, S. S-M. Lu, W. E. Miller, J. A. Moriarty, Appl. Phys. Lett. 32, 713 (1978).

2) A. Sher, United States Patent Gazette, 969, 725 (11 April 1978).

3) A. Sher, United States Patent Gazette, 971, 1215 (20 June 1978).

4) P. R. Bratt, Semiconductors and Semimetals, Vol. 12, Ed. by R. K. Willardson and A. C. Beer (Academic Press, New York, 1977) p. 39. See especially p. 102.

Publications Related to Activities Covered by the Grant

1) Photocapacitive MIS Infrared Detectors,

A. Sher, R. K. Crouch, S. S-M. Lu, W. E. Miller, J. A. Moriarty

Appl. Phys. Lett., 32, 713 (1978).

2) Photocapacitive Infrared Detectors,

A. Sher, S. S-M. Lu, J. A. Moriarty, R. K. Crouch, W. E. Miller

Bull. Am. Phys. Soc., 23, 226 (1978).

3) Apparatus for Converting Radiant Energy to Electric Energy,

A. Sher

United States Patent Gazette, 969, 725 (11 April 1978).

4) Solar Energy Converter,

A. Sher

United States Patent Gazette, 971, 1215 (20 June 1978).

5) $LaF_3$ Insulators Used to Improve MIS Structure Interface State Measurements,

A. Sher, Y. H. Tsuo, J. A. Moriarty, W. E. Miller, R. K. Crouch, B. A. Seiber

Bull. Am. Phys. Soc., 24, 496 (1979).

6) $LaF_3$ Insulators for MIS Structures,

A. Sher, W. E. Miller, Y. H. Tsuo, J. A. Moriarty, R. K. Crouch, B. A. Seiber

Appl. Phys. Lett. (accepted).

7) Si and GaAs Photocapacitive MIS Infrared Detectors,

A. Sher, Y. H. Tsuo, J. A. Moriarty, W. E. Miller, R. K. Crouch

Jour. Appl. Phys. (submitted).

8) Photocapacitive Infrared Detector and Solar Cell,

A. Sher, W. E. Miller, Y. H. Tsuo, R. K. Crouch, J. A. Moriarty

NASA Tech. Brief LAR-12345 (in print).

9) Improved Insulator Layer for MIS Devices,

A. Sher, W. E. Miller

NASA Tech. Brief LAR-12455 (in print).

## Invention Disclosures

1) $LaF_3$ Infrared Detectors and Solar Cells, A. Sher, 3 January 1978.

2) Radiant Energy to Electric Energy Converter Using Sintered Superionic Conductors, A. Sher, 25 March 1978.

3) Improved Insulating Layers for MIS Devices, A. Sher, W. E. Miller, 19 June 1978.

4) Photocapacitive Image Converter (CAPICON), A. Sher, W. E. Miller, Y. H. Tsuo, 26 September 1978.

5) Photocapacitive Image Converter II (PIC), A. Sher, W. E. Miller, 19 June 1978.

# APPENDIX A

## $LaF_3$ Insulators for MIS Structures

# $LaF_3$ INSULATORS FOR MIS STRUCTURES

A. Sher, College of William and Mary, Williamsburg, Virginia 23185

W. E. Miller, NASA-Langley Research Center, Hampton, Virginia 23665

Y. H. Tsuo, College of William and Mary, Williamsburg, Virginia 23185

John A. Moriarty, College of William and Mary, Williamsburg, Virginia 23185

R. K. Crouch, NASA-Langley Research Center, Hampton, Virginia 23665

B. A. Seiber, Virginia Commonwealth University, Richmond, Virginia 23284

## ABSTRACT

Thin films of $LaF_3$ deposited on Si or GaAs substrates have been observed to form blocking contacts with very high capacitances. This results in comparatively hysteresis-free and sharp C-V (capacitance-voltage) characteristics for MIS structures. Such structures have been used to study the interface states of GaAs with increased resolution and to construct improved photocapacitive infrared detectors.

Lanthanum floride ($LaF_3$) is a fast ionic conductor with exceptional polarization properties.[1] When this material is deposited on a substrate by e-gun evaporation, the resulting film possesses thin dipole layers (~50-100Å) at its surfaces[2] which produce large capacitive effects. In MIS structures, the film also acts as a blocking contact for electronic conduction as long as the breakdown voltage of the device is not exceeded. The effective capacitance of the film is that of an insulating layer 100-200Å thick with a dielectric constant of 14 (the bulk value of $LaF_3$). This capacitance is independent of the film's actual thickness as long as the measurement frequency lies below a characteristic value corresponding to the RC time constant of the $LaF_3$. For a typical 250Å film at room temperature, we have established that the characteristic frequency is above 100 kHz. At high enough frequencies, or at low temperatures where the ionic conduction ceases, the film's capacitance is expected to decrease to its geometrical value.

We have deposited $LaF_3$ films on freshly-prepared bare Si (n-type, with a carrier concentration $n \cong 3 \times 10^{14} cm^{-3}$), on freshly-prepared bare GaAs (n-type, with $n \cong 2 \times 10^{15} cm^{-3}$), and on native-oxide-coated Si and GaAs to form composite insulators.[3] The native oxide is thermally-grown $SiO_2$ on the former and anodized GaAs on the latter. Back ohmic contacts are formed for the Si samples by first e-beam depositing an Al film then sintering at 550°C for 10 minutes in flowing $N_2$ gas, and for the GaAs samples by e-beam depositing a film of Ge-Au-Ni alloy then sintering at 450°C for 10 minutes in flowing forming gas. Next the $LaF_3$ layer and a 125Å-thick transparent Au front contact are deposited to complete the MIS structure. Finally, the sample is annealed at 400°C in a $N_2$ atmosphere for one hour.

Measured C-V (capacitance-voltage) characteristics are illustrated for two Si samples in Fig. 1 and for two GaAs samples in Fig. 2. No visable hysteresis is observed in the Si characteristics. There is a small amount of hysteresis in the GaAs characteristics, but this is considerably less than that reported for anodized native-oxide layers alone.[4] The GaAs devices began to leak above the largest positive voltages shown (~ 1 volt) in Fig. 2. The Si sample with a 500Å layer of $LaF_3$ also began to leak above 0.8 volts, and the apparent onset of saturation above 0.4 volts is, in fact, due to the onset of this leakage instead.

The C-V characteristic for the composite-insulator-covered Si sample was measured at both 1 kHz and 100 kHz, as indicated in Fig. 1. In each case a saturation capacitance (the insulating-layer value) of 117 $nF/cm^2$ and a maximum/minimum capacitance ratio of 23 was obtained. Since the theoretical capacitance of a 250Å layer of $SiO_2$ is 136 $nF/cm^2$, we infer that the 250Å of $LaF_3$ contributes ~ 840 $nF/cm^2$. This corresponds to ~ 75Å surface dipole layers or an effective thickness for the $LaF_3$ film of ~ 150Å. (In other samples, effective thicknesses of ~ 120Å have been found.) The slight frequency dependence of the total capacitance at small bias voltages is most likely due to Si-$SiO_2$ interface-state effects,[5,6] but there may also be a contribution from slow surface states in the $LaF_3$.[1]

The C-V characteristic for the composite-insulators-covered GaAs sample in the depletion/inversion region is qualitatively similar to that of native-oxide-covered, n-type GaAs.[4] For a negative-voltage ramp, the capacitance falls below its equilibrium high-frequency value as the inversion region is approached. When the ramp is reversed, the capacitance rises to its equilibrium value (reaching it at -0.5 V in Fig. 2) and maintains this value back to zero bias. There are a number of possible explanations for

this effect. Previous workers have speculated on the existence of bulk traps[7] or a spatially-extended interface region between the GaAs and the native oxide[4] to account for the phenomenon. Another possibility is a long, insulator-dependent time constant for the generation of the holes needed to form the inversion layer.[8] Since replacing the native oxide by $LaF_3$ removes the effect, our results suggest that bulk traps are not the primary mechanism and that the proper explanation is linked to the properties of the insulating layer.

The effectively-thin insulating layers permitted by the use of $LaF_3$ would seem to have many potential device applications, e.g., CCD's with lower voltages or smaller areas needed to store a given charge and more sensitive, larger-dynamic-range varactors. Our direct interest in these structures, however, has been stimulated by two other types of application. The first is as an aid to the fundamental study of interface states, especially in GaAs where such states are not well characterized. The higher insulator capacitances permit higher resolution of interface-state effects in electrical measurements than otherwise possible. The second application is to improve photocapacitive MIS infrared detectors.[9]

As an illustration of the first application, we have plotted in Fig. 3 our measurements of the frequency and optical flux ($\Phi$) variation of the total series capacitance $C_S$ and dissipation factor D of the $LaF_3$-coated GaAs sample under zero applied bias voltage and subject to illumination on the front surface. The measured values of $C_S$ and D are observed to be independent of the wavelength of the incident light as long as the absorption depth of the semiconductor remains within an order of magnitude of the depletion-layer thickness. The data

in Fig. 3 was all taken at a wavelength of 0.820 μm. The solid lines in the figure are parameterized fits to the experimental points obtained from the equivalent circuit shown in the inset. Most of the circuit elements have a simple physical interpretation: $R_o$ is the sheet resistance of the front Au contact; $C_o$ is the insulator capacitance; $C_d$ is the depletion-layer capacitance of the semiconductor; and $C_i$ and $R_i$ are the interface-state capacitance and resistance. The remaining circuit elements $C_1$ and $R_1$ represent a yet undetermined process, but probably a secondary one associated with the insulator-GaAs interface. The isolation of $C_i$ and $R_i$ allows one to immediately infer the interface-state density at the Fermi level, $N_i$, by the relationship[5]

$$N_i = C_i/eA \quad ,$$

where A is the device area, and also the interface-state response time constant

$$\tau_i = R_i C_i \quad .$$

Only $C_d$ and $\tau_i$ vary significantly with light intensity. The former increases with $\Phi$ because electron-hole pairs created by the photons absorbed in the depletion layer are separated by its large electric field thereby decreasing its thickness. The interface-state response rate $\tau_i^{-1}$ increases linearly with $\Phi$,

$$\tau_i^{-1} = \tau_{io}^{-1} + K_i\Phi \quad ,$$

because light-generated holes are driven to the interface by the depletion-layer electric field, thus providing a fast exit mechanism for electrons localized in interface states. Numerical values of the fitted circuit parameters for both the $LaF_3$-coated and composite-insulator-coated GaAs samples are given in the Table.

The fitting procedure itself starts by assigning a value to $C_o$ that is inferred from the measured insulator-layer thicknesses and known dielectric constants. Then $C_d$ is obtained for the different light intensities from the high-frequency $C_s$ measurements where $C_s^{-1} \cong C_o^{-1} + C_d^{-1}$. Next, $C_i$ can be determined from the low-frequency, high-light-intensity data since here $C_s^{-1} \cong C_o^{-1} + (C_i + C_d)^{-1}$. The parameters $C_1$ and $R_1$ are needed to fit the low-light-intensity dissipation factor data between $10^2$ and $10^3$Hz, and are responsible for the upward inflection of the curves in this region. The resistance $R_o$ is then established from the high-frequency behavior of D. Finally, the values of $\tau_i$ are adjusted to fit the light dependence of the $C_s$ and D curves, resulting in the linear dependence on $\Phi$ given above. The least well-known parameter in this procedure is $C_o$. However, since it is so large it has relatively little effect on the other parameters. The quantity most effected by the uncertainty in $C_o$ is $C_i$. The $C_o$ used in Fig. 3 (320 nf) corresponds to an effective thickness for the $LaF_3$ layer of ~ 120Å. If the appropriate thickness were 150Å instead, then $C_o$ = 250 nf and $C_i$ changes from 170 nf to 202 nf, suggesting about a 15% uncertainty. However, with the same $C_o$ variation, $C_d$ changes from 5.571 nf (in the dark) to 5.598 nf, for only about a 0.5% uncertainty. The time constants $\tau_i$ and $\tau_1$ are also insensitive to $C_o$ provided it is large. If, on the other hand, a 1000Å native-oxide layer were used, then $C_o$ would be only ~ 20 nf, and if, in addition, a more typical carrier concentration[6] of $2 \times 10^{16} cm^{-3}$ were used, then $C_d$ would be ~ 15 nf. The result of having $C_o \sim C_d$ is to compress the maximum variation in $C_s$ by more than an order of magnitude, thus greatly decreasing the resolution of the measurement.

We have made similar measurements of $C_S$ and D on low-carrier-concentration Si samples. In this case $C_1$ and $C_d$ have comparable magnitudes and their contributions to the total parallel conductance $G_p$ are easily identified, i.e., $G_p/\omega$ vs. frequency plots[5,10] have two well-resolved peaks. The main peak in the dark, lies at low frequency, less than 1 Hz. The secondary peak is an order of magnitude smaller than the primary one, and is at 3.3 kHz. The density of states associated with the new peak is $N_1 \cong 3.9 \times 10^{10}$ states/eV-cm$^2$. This new peak is not the high frequency peak ($\sim 10^7$ Hz) reported by Morita et al.[11] This data will be presented in detail elsewhere.

In the general case, one can identify four features of our MIS structures and measurement technique which lead to improved resolution of interface-state effects:

(i) The large values of $C_o$ permitted by the effectively thin insulating layers maximize the interface/semiconductor contribution to the measured electrical quantities.

(ii) The use of low-carrier-concentration semiconductors keeps $C_d$ relatively small, so there is less shunt effect on the $C_i$, $R_i$ and $C_1$, $R_1$ legs of the circuit. The carrier concentrations of our samples are significantly lower than those normally used heretofore.[6]

(iii) The measurement of $C_S$ and D as a function of optical flux helps to identify $C_i$ and $R_i$.

(iv) The comparison of the behavior of different insulators helps to distinguish different physical mechanisms, especially bulk and interface effects.

To this list we could also add the temperature and bias voltage variation of $C_S$ and D. We expect, for instance, that such measurements will be useful in refining our understanding of the GaAs interface-state properties and ultimately providing a complete profile of the interface density of states.

In our second application, photocapacitive MIS infrared detectors[9] that operate at room temperature have been built from both $LaF_3$-covered and composite-insulator-covered Si and GaAs. These new detectors have unoptimized detectivities at 13 Hz of $\sim 2 \times 10^{13} W^{-1}$-cm-$Hz^{\frac{1}{2}}$ for Si and $\sim 1 \times 10^{13} W^{-1}$-cm-$Hz^{\frac{1}{2}}$ for GaAs. The former number represents an order-of-magnitude improvement over both our initial Si devices,[9] which used $SiO_2$ insulating layers, and conventional photovoltaic Si detectors.[12] Additional details on this application will also be presented elsewhere.

Finally, we should mention that a preliminary study of the compatibility of $LaF_3$ films with photolithography techniques has also been conducted. Two $SiO_2$-$LaF_3$ composite insulator samples were treated. A mesa was made on one, and a hole in the composite layer was etched into the other with HCl. This experience indicates that the use of $LaF_3$ films on Si is compatible with standard microcircuit fabrication techniques.

## ACKNOWLEDGMENTS

We wish to thank W. R. Feltner who grew the $SiO_2$ layers, and T. C. Steele for his help with sample preparation.

## REFERENCES


1. A. Sher, R. Solomon, K. Lee and M. W. Muller, Phys. Rev. 144, 593 (1966); R. Solomon, A. Sher and M. W. Muller, J. Appl. Phys. 37, 3427 (1966).
2. C. O. Tiller, A. C. Lilly and B. C. LaRoy, Phys. Rev. B8, 4787 (1973); B. C. LaRoy, A. E. Lilly and C. O. Tiller, J. Electrochem. Soc. 120, 1668 (1973).
3. The oxide coated Si was supplied to us by W. R. Feltner of the Electronics Development Division of the NASA Marshall Space Flight Center. The GaAs, purchased from Applied Materials, is a 20 μm thick Te-doped epitaxial layer on an $n^+$ substrate.
4. E. Kohn and H. L. Hartnagel, Solid State Elec. 21, 409 (1978).
5. The physics of MIS devices is reviewed by S. M. Sze, Physics of Semiconductor Devices (Wiley, New York, 1969) pp. 425-504.
6. A. Goetzberger, E. Klansmann, M. J. Schulz, CRC Critical Reviews in Solid State Sci., 6, 1 (1976).
7. C. R. Zeisse, L. J. Messick and D. L. Lile, J. Vac. Soc. Technol. 14, 857 (1977).
8. A. Goetzberger, IEEE Transactions on Electron Devices, ED-14, 782 (1967).
9. A. Sher, R. K. Crouch, S. S.-M. Lu, W. E. Miller, J. A. Moriarty, Appl. Phys. Lett. 32, 713 (1978).
10. E. H. Nicollian and A. Goetzberger, Bell Sys. Tech. Jour. 6, 1055 (1967).
11. M. Morita, K. Tsubouchi and N. Mikoshiba, Appl. Phys. Lett. 33, 745 (1978).
12. H. Levinstein, in Semiconductors and Semimetals, edited by R. K. Willardson and A. C. Beer (Academic, New York, 1970), vol. 5, p. 10.

TABLE: EQUIVALENT CIRCUIT PARAMETERS FOR GaAs MIS STRUCTURES

| | 250Å Native Oxide + 500Å $LaF_3$ | | | | 250Å $LaF_3$ | | | | |
|---|---|---|---|---|---|---|---|---|---|
| filter | $10^{-3}$ | $10^{-2}$ | $10^{-1}$ | $10^{0}$ | dark | $10^{-3}$ | $10^{-2}$ | $10^{-1}$ | $10^{0}$ |
| $\Phi(cm^{-2}\text{-}sec^{-1})$ | $1.13\times10^{10}$ | $1.43\times10^{11}$ | $8.59\times10^{11}$ | $8.76\times10^{12}$ | - | $1.13\times10^{10}$ | $1.43\times10^{11}$ | $8.59\times10^{11}$ | $8.76\times10^{12}$ |
| $C_d$(nF) | 5.03 | 5.05 | 5.17 | 5.37 | 5.571 | 5.579 | 5.764 | 5.962 | 6.224 |
| $\tau_i$(sec) | 0.38 | 0.27 | 0.097 | 0.012 | 3.00 | 2.20 | 0.970 | 0.202 | 0.0215 |
| $C_o$(nF) | 85 | | | | 320 | | | | |
| $R_o(\Omega)$ | 28.3 | | | | 13.8 | | | | |
| $C_i$(nF) | 105 | | | | 170 | | | | |
| $N_i$(states/eV-$cm^2$) | $2.9\times10^{12}$ | | | | $3.54\times10^{12}$ | | | | |
| $\tau_{io}$(sec) | 0.411 | | | | 2.81 | | | | |
| $K_i(cm^2)$ | $9.23\times10^{-12}$ | | | | $5.27\times10^{-12}$ | | | | |
| $C_1$(nF) | 0.12 | | | | 0.068 | | | | |
| $\tau_1$(sec) | $1.7\times10^{-4}$ | | | | $2.5\times10^{-4}$ | | | | |

## FIGURE CAPTIONS

Figure 1.- The C-V characteristics for two Si samples. The ramp rate for all curves is ~50mV/sec.

Figure 2.- The C-V characteristics for two GaAs samples. The ramp rate for both curves is ~50mV/sec.

Figure 3.- The series capacitance $C_S$ and dissipation factor D as a function of frequency and photon flux for the GaAs sample with a 250Å-thick $LaF_3$ insulator. The dots are data points and the solid curves are fits to these points determined by inserting the parameters in the Table into analytic expressions for $C_S$ and D for the circuit shown in the inset.

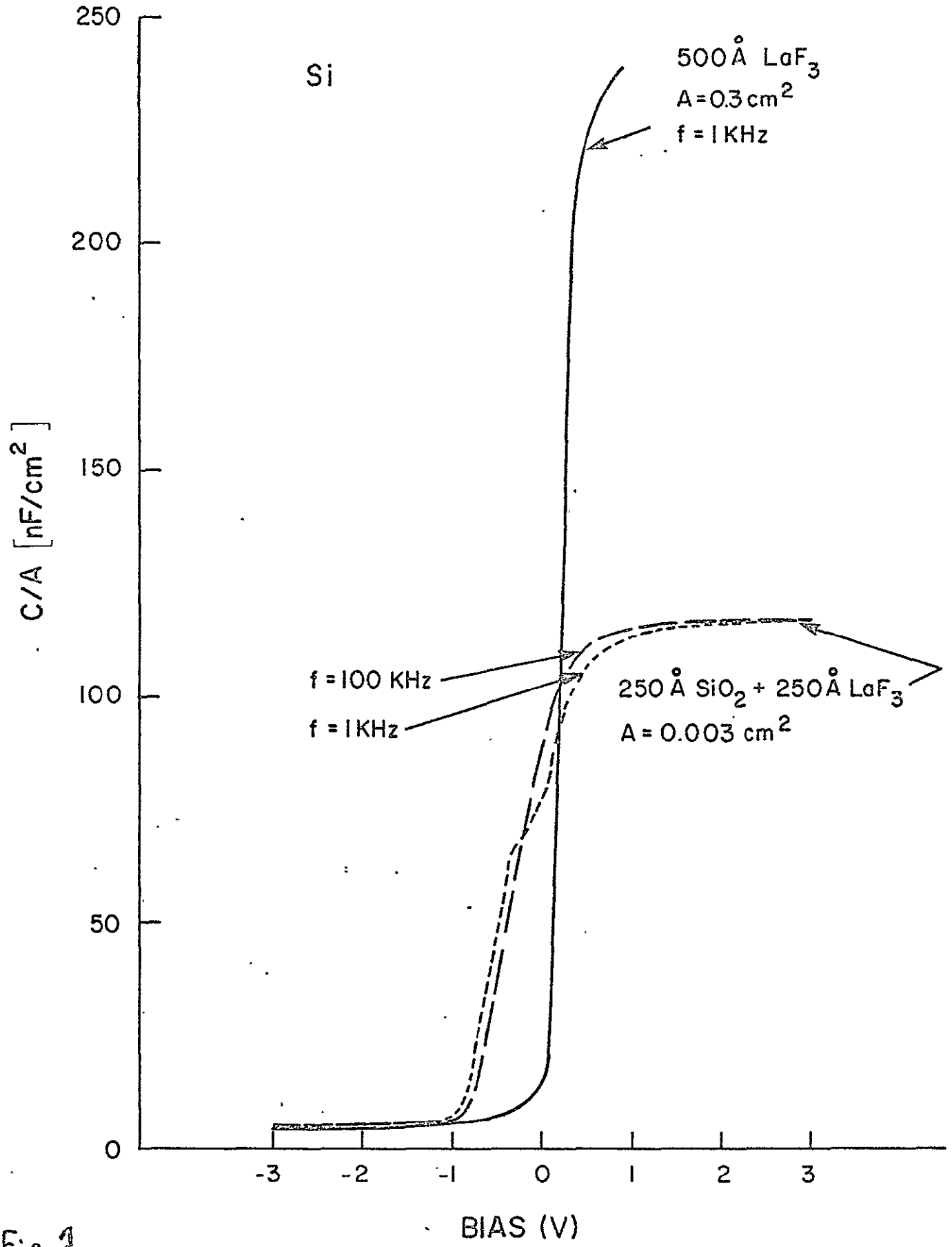
Si
500 Å LaF3
A = 0.3 cm2
f = 1 KHz
f = 100 KHz
f = 1 KHz
250 Å SiO2 + 250 Å LaF3
A = 0.003 cm2
C/A [nF/cm2]
250
200
150
100
50
0
-3
-2
-1
0
1
2
3
BIAS (V)

Fig 2

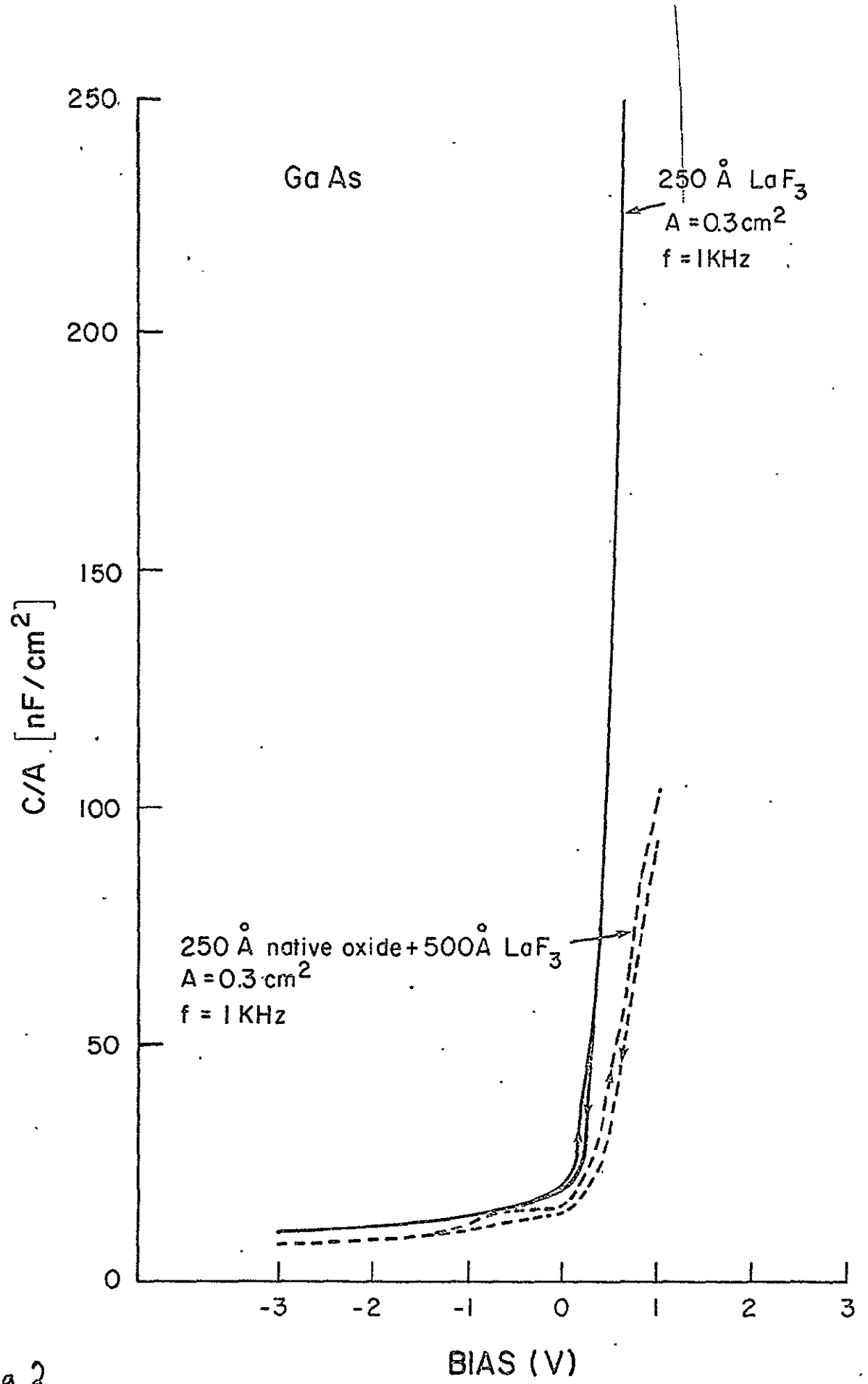
Ga As
250 Å LaF3
A = 0.3 cm2
f = 1 KHz
250 Å native oxide + 500Å LaF3
A = 0.3 cm2
f = 1 KHz
C/A [nF/cm2]
250
200
150
100
50
0
-3
-2
-1
0
1
2
3
BIAS (V)

Fig 2

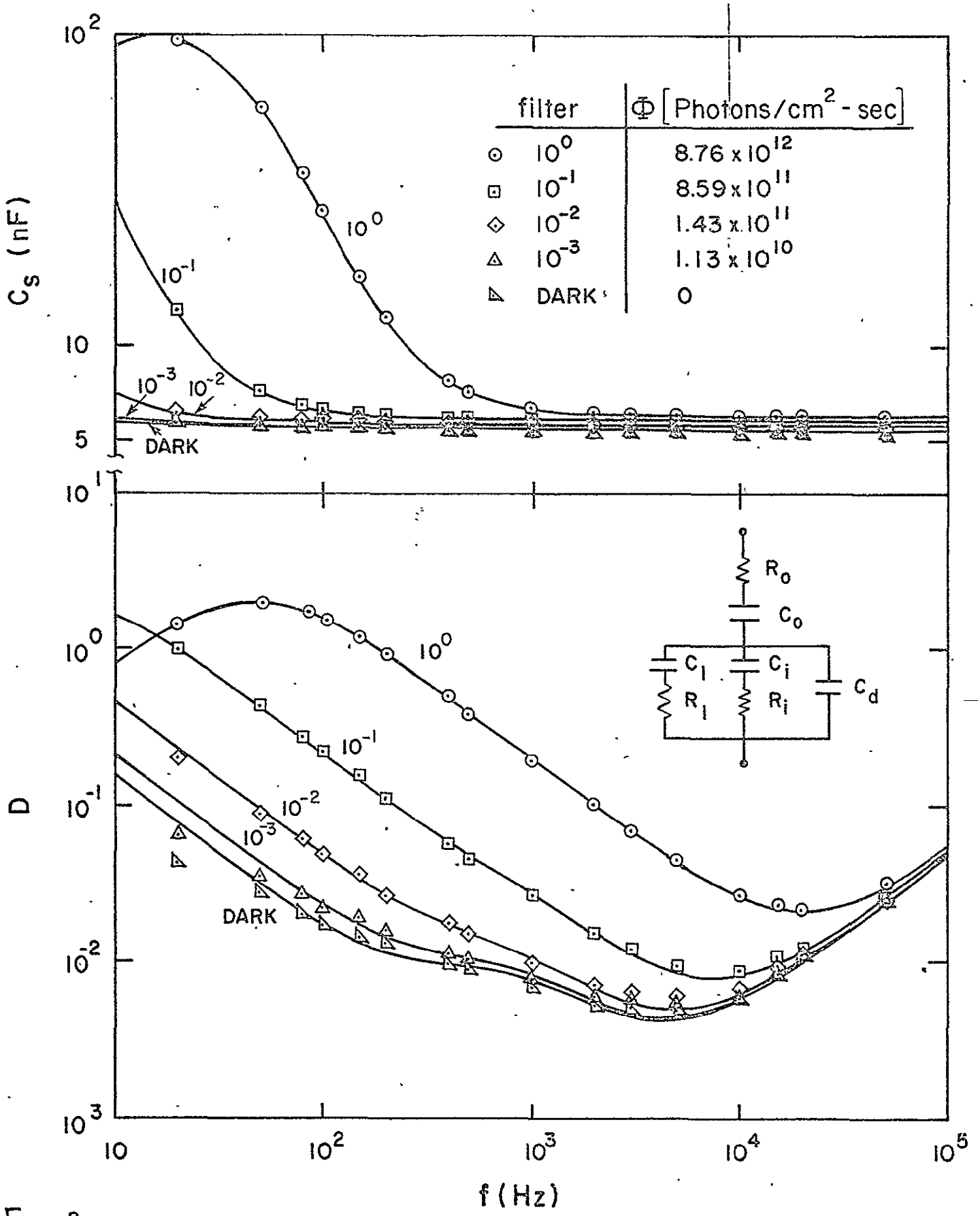

filter
Φ [Photons/cm² - sec]
10⁰ 8.76 x 10¹²
10⁻¹ 8.59 x 10¹¹
10⁻² 1.43 x 10¹¹
10⁻³ 1.13 x 10¹⁰
DARK 0
Cs (nF)
D
f (Hz)
DARK
R0
C0
C1
R1
Ci
Ri
Cd


Fig 3

# APPENDIX B

## Si and GaAs Photocapacitive MIS Infrared Detectors

# Si and GaAs Photocapacitive MIS Infrared Detectors

A. Sher, Y. H. Tsuo, John A. Moriarty
College of William and Mary, Williamsburg, Virginia 23185

W. E. Miller, R. K. Crouch
NASA-Langley Research Center, Hampton, Virginia 23665

ABSTRACT

Improvement of the previously-reported photocapacitive MIS infrared detectors has led to the development of exceptional room-temperature devices. Unoptimized peak detectivities on the order of $10^{13}W^{-1}cmHz^{1/2}$, a value which exceeds the best obtainable from existing solid-state detectors, have now been consistently obtained in Si and GaAs devices using high-capacitance $LaF_3$ or composite $LaF_3$/native-oxide insulating layers. The measured spectral response of representative samples is presented and discussed in detail together with a simple theroy which accounts for the observed behavior. The response of an ideal MIS photocapacitor is also contrasted with that of both a conventional photoconductor and a p-i-n photodiode, and reasons for the superior performance of our detectors are given. Finally, fundamental studies on the electrical, optical and noise characteristics of our MIS structures are analyzed and discussed in the context of infrared-detector applications.

## I. INTRODUCTION

In an earlier paper[1] we reported on a new class of room-temperature infrared detectors, which exploits the normal photocapacitive effect in MIS (metal-insulator-semiconductor) systems[2], and our initial measurements on prototype Si devices. Since that time, we have achieved an order-of-magnitude improvement in the performance of these detectors. Although our current Si and GaAs devices are still unoptimized, they now outperform comparable solid-state detectors[3] with peak detectivities on the order of $10^{13} W^{-1} cm Hz^{1/2}$. In this paper we wish to give a full account of our latest experimental findings on Si and GaAs photocapacitive MIS infrared detectors.

The mechanism we are exploiting in infrared detection is very general and applies to a wide range of dielectric materials. In all cases, operation depends on arranging the material so that its electrical capacitance varies as modulated light impinges on it. If the capacitor is charged initially (by an external source, or because of work-function differences between the contacts, or because of stored surface charges), then the time-varying capacitance generates a voltage across the device, which can be detected in a suitable external circuit. In the photocapacitive mode of operation, the capacitance is varied through processes which depend sensitively on the wavelength of the incident radiation, e.g., the creation of electron-hole pairs. In nearly intrinsic semiconductors, therefore, the wavelength must be shorter than that corresponding to the energy gap, as in conventional photoconductive and photovoltaic devices, and a narrow-band sensor results. In our typical Si detectors, the detecitvity peaks at

a wavelength near 0.9 μm and falls to one-half its peak value at about 0.5 μm and 1.0 μm.

Semiconductors to be operated in the photocapacitive mode are optimally arranged in an MIS configuration.[1] Device performance is influenced by the choice of metal contacts and the insulating material as well as the semiconductor used. The back ohmic contact and the front transparent metal contact can be made of metals whose work-function difference biases the device into depletion or inversion. Thus, the desired charged capacitor can be created without an external applied voltage. For the insulating layer, a number of different materials have been tried. The best ones have proven to be native oxides of the semiconductor being used and electron-beam deposited lanthanum floride ($LaF_3$) films, or combinations of the two[4]. The native oxide of silicon ($SiO_2$) can be thermally grown, while the GaAs may be anodized to form its native oxide. The $LaF_3$ film has the useful property of possessing a high fixed capacitance independent of its actual thickness (250-1000Å), provided that the modulation frequency is below a characteristic response frequency (> 100 kHz). Such a film acts as though it were 100-200Å thick with a dielectric constant of 14 (the bulk value of $LaF_3$). The presence of $LaF_3$ also permits a blocking front contact to be achieved with much thinner native-oxide layers (100-250Å) than otherwise possible.

In Sec. II we present and discuss our experimental measurements of the responsivity and detectivity for representative Si and GaAs devices. A simple theory of the responsivity is also developed there and used to contrast the photocapacitive-mode performance with that of photoconductive and photovoltaic devices. In Sec. III we discuss additional fundamental studies on our

MIS structures, including the determination of the equivalent circuit, the precise relation between the measured and generated signal voltage, the sources of noise in these devices, and the optimization of the detectivity. Concluding remarks are given in Sec. IV.

## II. RESPONSIVITY AND DETECTIVITY

### A. Experimental Measurements

We have constructed in excess of twenty Si and GaAs MIS photocapacitive infrared detectors with normalized peak detectivities $D_\lambda^*$ on the order of $10^{13} W^{-1} cmHz^{1/2}$.[5] Out of these we have chosen three representative samples (to be denoted as Si-58, GaAs-7 and GaAs-10) for extended analysis and discussion here. For future reference some of the important physical parameters of these samples are summarized in Table I. In each case the MIS structure consists of a 125Å-thick transparent Au front contact followed by either a single insulating layer of $LaF_3$ or a double layer of $LaF_3$ and native oxide adjacent to the semiconductor. In the latter case, the $LaF_3$ is deposited directly on top of native-oxide-coated Si or GaAs, while in the former, the $LaF_3$ is deposited on freshly-prepared bare Si or GaAs. Low-carrier-concentration, n-type semiconducting material is used in all samples, with the (100) surface in Si and (111) surface in GaAs exposed to the insulating layer. Back ohmic contacts are formed for the Si samples by first e-beam depositing an Al film then sintering at 550°C for 10 minutes in flowing $N_2$ gas, and for the GaAs samples by e-beam depositing a film of Ge-Au-Ni alloy then sintering at 450°C for 10 minutes in flowing forming gas. The completed MIS structure is annealed at 400°C in a $N_2$ atmosphere for one hour.

The normalized responsivity[6]

$$R_\lambda^* = V_s / P_0 \qquad (V\text{-}cm^2/W) \tag{1}$$

and detectivity

$$D_\lambda^* = \frac{V_s}{V_n} \frac{(\Delta f)^{1/2}}{P_0 A^{1/2}} \qquad (W^{-1} cm\ Hz^{1/2}) \tag{2}$$

for our three samples have been determined by shining modulated, monochromatic light on the top Au contact of the MIS structure and measuring the resultant signal voltage $V_s$. Plots of $R_\lambda^*$ and $D_\lambda^*$ as a function of optical intensity and wavelength $\lambda$ are shown in Figs. 1-3. These measurements all refer to the following experimental conditions: room temperature; no externally applied bias; modulation or chopping frequency $f = 13$ Hz; amplifier band width $\Delta f = 0.53$ Hz; and monochrometer slit width 2mm (spectral resolution ~ 100Å). The measured noise voltages $V_n$ are listed in Table I, and average photon flux $\Phi$ and power density $P_0$ values for the various optical filters used are given in Table II.

It can be seen from Figs. 1-3 that in general detector response at a given wavelength decreases as the radiation intensity is increased, although at the lowest light levels used an approximate linear-response regime exists. Saturation of the detector will occur at high light levels, but its onset is clearly very slow, with $R_\lambda^*$ and $D_\lambda^*$ decreasing by less than an order of magnitude for a 1000-fold increase in $P_0$. The long-wavelength cutoff of the response reflects the absorption characteristics of the semiconductor used. Thus devices fabricated from GaAs, which is a direct-band-gap material, exhibit much sharper cutoffs below their threshold wavelength than do those of Si, which is an indirect-band-gap material. Below the wavelength of peak responsivity, both materials have a region where $R_\lambda^*$ falls roughly as $1/\lambda$, which means that the response per photon is nearly constant. Both materials also exhibit a small auxillary peak centered near $\lambda = 0.5$ μm, beyond which $R_\lambda^*$ falls off sharply at still shorter wavelengths. The auxillary peak is quite likely related to the sharp increase in the transmission coefficient of Au films below $\lambda = 0.6$ μm.[7]

## B. Simple Theory for $R_\lambda^*$

A complete description of the photocapacitive response of MIS systems requires a careful account of the generation, transport, and recombination of electrons and holes at the insulator-semiconductor interface and throughout the entire space-charge region of the semiconductor. Such an analysis is in progress, but the essence of the phenomenon can be understood in terms of a simple model for the photoresponse of an ideal depletion-layer. Moreover, the generated signal voltage $V_s^0$ obtained from this model can be conveniently related to the measured signal voltage $V_s$ through the appropriate equivalent circuit of the device and measuring apparatus, as discussed in Sec. III.

Consider an ideal MIS structure (i.e., one without interface states or fixed charges) containing n-type semiconducting material and internally biased into depletion or inversion. If the device is in inversion, the modulation frequency will be taken as fast compared to the effective minority-carrier generation rate, so that the inversion-layer charge does not respond to the external stimulus. Ignoring the inversion layer, the total voltage across the device is just

$$V = \frac{Q}{C_0} + \psi_s \quad , \tag{3}$$

where Q is the total amount of charge depleted from the semiconductor,

$$Q = -e\, n_b\, \ell_d\, A \quad , \tag{4}$$

with $n_b$ the bulk carrier concentration, A the active area, and $\ell_d$ the depletion-layer thickness; $C_0$ is the insulating-layer capacitance; and $\psi_s$ is the potential at the insulator-semiconductor interface,

$$\psi_s = -\frac{1}{2}\frac{e}{\varepsilon_s} n_b \ell_d^2 \quad , \tag{5}$$

with $\varepsilon_s$ the dielectric constant of the semiconductor (in units of $\varepsilon_o$). The estimated surface potentials[8] present in our three samples are given in Table I. In the case of Si-58, $\psi_s$ corresponds to weak inversion, while in both GaAs samples, which do not form inversion layers, $\psi_s$ corresponds to a region of deep depletion.

We next envisage low intensity, monochromatic radiation, modulated at a frequency $f = \omega/2\pi$, to be normally incident on the front metal contact of the device. Electron-hole pairs are generated in the semiconductor at a rate (per unit area) of

$$g_\lambda = \frac{\eta_\lambda P_o}{E_\lambda}\left(1 + e^{i\omega t}\right) \quad , \tag{6}$$

where $\eta_\lambda$ is the fraction of photons actually absorbed by the semiconductor (i.e., the quantum efficiency) and $E_\lambda = hc/\lambda$ is the quantum of photon energy. The effective recombination time for these pairs, $\tau_\lambda$, will depend on the spacial region of the semiconductor in which they are created. If $\lambda$ is either far below or just below threshold, corresponding to pair production at the insulator-semiconductor interface or well into the bulk, respectively, then $\tau_\lambda$ will be very short and the depletion layer unaffected. In the former case recombination is speeded by the high density of surface states or traps at the interface, while in the latter case $\tau_\lambda$ approaches the bulk minority carrier lifetime $\tau_p$. For intermediate wavelengths, however, the electron-hole pairs will be created in the large electric field of the depletion layer. In this case the holes are driven to the interface and the electrons to the

back of the depletion layer before they can recombine. The depletion layer is consequently thinned and its capacitance increased by the radiation. Recombination can now occur only by thermal diffusion of electrons and holes against the depletion-layer field, a very slow process. In this regime, $\tau_\lambda \gg \tau_p$ and $\omega\tau_\lambda \gg 1$. If little charge flows in the external circuit compared to that which flows across the depletion layer, then a voltage $\delta V$ develops across the device. From Eqs. (3) and (5) with Q constant, one has

$$\begin{aligned} \delta V &= \delta \psi_s \\ &= -\frac{e}{\varepsilon_s} n_b \ell_d \, \delta \ell_d \end{aligned} \quad . \tag{7}$$

The change in the depletion-layer thickness, $\delta\ell_d$, may be related to the number of electrons created by the radiation field, $\delta N$, by the conservation of charge:

$$\delta Q = -e n_b \delta \ell_d A - e \delta N = 0 \quad . \tag{8}$$

In turn, $\delta N$ is governed by the simple rate equation

$$\frac{d\,\delta N}{dt} = g_\lambda A - \frac{\delta N}{\tau_\lambda} \quad , \tag{9}$$

whose solution, using Eq. (6), is

$$\delta N = \frac{\eta_\lambda P_0 \tau_\lambda A}{E_\lambda} \left[ 1 + \frac{1}{1 + i\omega\tau_\lambda} e^{i\omega t} \right] \quad . \tag{10}$$

Combining Eqs. (7), (8) and (10), one finds

$$\delta V = \frac{\eta_\lambda P_0 \tau_\lambda e A}{E_\lambda C_d} \left[ 1 + \frac{1}{1 + i\omega\tau_\lambda} e^{i\omega t} \right] , \tag{11}$$

where

$$C_d = \frac{\varepsilon_s A}{\ell_d} \tag{12}$$

is the depletion-layer capacitance. Clearly, $\delta V \to 0$ when $\tau_\lambda \to 0$ as physically argued above. In the region of principal interest where $\omega\tau_\lambda >> 1$, the magnitude $V_s^0$ and phase $\phi_s^0$ of the generated ac signal voltage $V_s^0 e^{i(\omega t+\phi_s^0)}$ become

$$\begin{aligned} V_s^0 &= \frac{\eta_\lambda P_0}{E_\lambda} \cdot \frac{eA}{C_d \omega} \\ &= \frac{\eta_\lambda P_0}{hc}\left(\frac{-2e\psi_s}{n_b \varepsilon_s}\right)^{\frac{1}{2}} \frac{\lambda}{\omega} \end{aligned} \tag{13}$$

and

$$\begin{aligned} \phi_s^0 &= -\tan \omega\tau_\lambda \\ &\cong -\pi/2 \end{aligned} \tag{14}$$

The latter represents the usual $90^\circ$ phase lag expected from a capacitive response. In the special case of strong inversion, where $C_d$ and $\psi_s$ are constants independent of the bias, these results also agree with a limiting form of earlier expressions obtained by Nakhmanson.[10]

The responsivity of an ideal MIS photocapacitive detector,

$$R_\lambda^{*,0} = \frac{V_s^0}{P_0} \quad , \tag{15}$$

can be used to estimate the expected upper limit for real devices. For $\eta_\lambda = 1$, $\lambda = 0.82$ μm and f = 13 Hz, we find $R_\lambda^{*,0} = 11.4$, 4.4 and 4.8 x $10^5$V-cm$^2$/W for Si-58, GaAs-7 and GaAs-10, respectively, at zero applied bias. The low-intensity ($10^{-3}$ filter) measured values shown in Figs. 1-3 are within a factor of 3 of these limits for the GaAs samples, but about a factor of 10 smaller in Si-58. The latter primarily reflects a significant loading of the signal by the amplifier, as discussed in Sec. III.

The predicted dependences of the response on $\lambda$, $\psi_s$ and $\omega$ have also been examined. The linear variation of $R_\lambda^*$ and $D_\lambda^*$ with wavelength noted above is more clearly illustrated in Fig. 4, where we have plotted $R_\lambda^*/E_\lambda$ vs. $\lambda$ for GaAs-7. The predicted $\omega^{-1}$ frequency dependency has also been observed in the measured $R_\lambda^*$ at low light intensity, as shown in Fig. 5 for GaAs-10. The deviation at low frequency for the higher light intensities arises mostly from the difference in the measured and generated signal voltages, as discussed in Sec. III. Finally, the dependence of the response on surface potential has been investigated by measuring $V_s$ as a function of applied bias voltage. In the case of Si-58 only a semi-quantitative approximation to the expected behavior was found, but this included the anticipated saturation at large negative bias, where $\psi_s$ becomes constant. In GaAs, on the other hand, rather striking confirmation of the $(-\psi_s)^{1/2}$ dependence has been obtained, as shown in Fig. 6. Note that the apparent generated signal voltage $V_s^0$ rather than the directly measured $V_s$ is plotted here, using Eq. (26) of Sec. III.

An additional important aspect of Eq. (13), which we have anticipated in our experimental program, is the premium on low-carrier-concentration semiconducting material. Our carrier concentrations (see Table I) are significantly lower than used in most MIS applications heretofore, but we have not as yet sought the real practical limit to which this material parameter can be exploited. There is also, in principal, an equal premium on a low dielectric constant. In this case, however, the slight variation among useful semiconductors will almost certainly be overshadowed by other considerations, such as the wavelength of peak response.

C. Comparison with Photoconducting and p-i-n Devices

At this point it is instructive to compare $V_s^0$ for an ideal photocapacitor with the corresponding results for conventional photoconducting and p-i-n devices. The appropriate geometries of the three devices in the presence of incident radiation is indicated schematically in Fig. 7. As above, we consider the ideal high frequency open circuit signal voltage generated in response to low-intensity, modulated radiation. For simplicity and ease of comparison we assume that each device is held at a common bias voltage V and absorbs the incident radiation with equal quantum efficiency $\eta_\lambda$. The signal voltage $V_s^0$ in each case is most easily obtained from the general equivalent circuit also shown in Fig. 7. The appropriate values of the generated current density $J_s$, impedance Z, and $V_s^0$ are given in Table III. The term $\mu_e V/(\omega L_0^2)$ in $J_s$ for the photoconductor accounts for the number of electrons (with mobility $\mu_e$) that traverse the length $L_0$ in a chopping period $\omega^{-1}$, i.e., it is the photoconducting gain. The impedance of the photoconductor is just its geometrical resistance

$$R = \frac{L_0}{e\mu_e n_b A} \tag{16}$$

while that of the p-i-n photodiode arises from the capacitance associated with the intrinsic region

$$C_{Pin} = \frac{\varepsilon_s A}{\ell_i} \quad . \tag{17}$$

From Table III we may immediately obtain the desired ratios of signal voltages:

$$\frac{V^0_{s,pcap}}{V^0_{s,pc}} = \left|\frac{2\psi_s}{V}\right| \frac{L_0}{\ell_d}$$
$$\sim \frac{L_0}{\ell_d} \gg 1 \tag{18}$$

and

$$\frac{V^0_{s,pcap}}{V^0_{s,pin}} = \frac{\ell_i}{\ell_d} \sim 1 \quad . \tag{19}$$

Thus because $L \gg \ell_d, \ell_i$ both the photocapacitive and p-i-n detectors possess an inherent advantage over the photoconductor. The physical reason for this is that both capacitive devices are effectively able to store the entire generated charge on the capacitor in each cycle, which more than compensates for the gain factor in the generated current of the photoconductor.

A quantitative comparison of practical devices entails many additional considerations, of course, including differences in quantum efficiency, sources of noise, and the ease of fabricating the ideal geometry. Since the photocapacitive and p-i-n detectors must absorb the radiation in a relatively small volume to be effective, one expects

$$\eta_{\lambda,pc} > \eta_{\lambda,pcap} \sim \eta_{\lambda,pin} \quad . \tag{20}$$

This implies a broader wavelength response for the photoconductor, but probably little advantage near the region of peak response. The principal sources of noise in the three devices are rather different and more difficult to compare in a simple way. Both the photoconductor and the p-i-n detector, however, contain inherent noise sources even in the ideal operation envisaged above. In the former there is the usual thermal noise arising from the resistance R, while in the latter a shot noise will result from the dark current which flows through the intrinsic region. The ideal photocapacitor, on the

other hand, is essentially noiseless, with the leading source of noise in real devices arising from the resistance associated with insulator-semiconductor interface states and inversion layer, as discussed further in Sec. III. This ultimately means that the noise may be controlled through material parameters which do not affect the generated signal voltage, a decided advantage. Finally, the MIS geometry of the ideal photocapacitor, with no internal semiconductor junctions, is probably more closely approximated in practice than that of the p-i-n photodiode. The sum total of these considerations would seem to explain the superior performance we have achieved with our photocapacitive devices.

## III. FUNDAMENTAL STUDIES ON MIS STRUCTURES

### A. Determination of the Equivalent Circuit

To better understand the factors governing detector performance in the MIS photocapacitor, we have conducted a number of fundamental studies on our samples. Specifically, we have measured the frequency and dc optical flux ($2\Phi$) variation of the total series capacitance $C_s$ and dissipation factor D of Si-58, GaAs-7 and GaAs-10 in an effort to empirically determine the equivalent circuit of these devices.[4,11] Our results for the GaAs samples were discussed in Ref. 4 and $C_s$ and D for GaAs-7 are plotted in Fig. 3 of that paper. The corresponding results for GaAs-10 are illustrated in Fig. 8 together with the inferred equivalent circuit. In both GaAs samples the observed circuit is distinguished from that of an ideal photocapacitor (insulator capacitance $C_0$ in series with $C_d$) in three respects: (i) a small sheet resistance $R_0$ (10-30 Ω) arising from the large-area front Au contact; (ii) a large surface-state capacitance $C_{ss}$ (100-200 nF) and resistance $R_{ss}$ (0.1-20 MΩ) associated with the insulator-GaAs interface[12]; and (iii) a much smaller capacitance $C_1$ (~ 0.1 nF) and resistance $R_1$ (~ 2 MΩ) representing a secondary, but undetermined, interface process. (The latter parameters are needed to fit the slight upward inflection in D near $10^3$ Hz at low light intensity.) Of these circuit elements only $C_d$ and $R_{ss}$ were found to vary significantly with light intensity. The former increases by about 10% while the latter decreases by two orders of magnitude in going from the dark to the brightest light used. Numerical values of the circuit parameters are given in Ref. 4.

The fitting procedure itself starts by assigning a value to $C_0$ that is inferred from the insulator-layer thicknesses and known dielectric constants. Then, $C_d$ is obtained for the different light intensities from the high-frequency $C_s$ measurements where $C_s^{-1} \cong C_0^{-1} + C_d^{-1}$. Next, $C_{ss}$ can be determined from the low-frequency high-light-intensity data since here $C_s^{-1} \cong C_0^{-1} + (C_{ss} + C_d)^{-1}$. Additional circuit parameters ($R_0$, $C_1$ and $R_1$ in the case of GaAs) are introduced, as required, to fit the low-light-intensity dissipation factor. Finally, $C_d$ and the interface-state resistance $R_{ss}$ are allowed to vary with light intensity as needed to accommodate the light-dependence of the $C_s$ and D curves. One of the least well known parameters in this procedure is $C_0$. However, since it is large it has relatively little effect on the other parameters. The quantity most affected by the uncertainty in $C_0$ is $C_{ss}$. In GaAs-7, for example, if $C_0$ were decreased from 320 nF to 250 nF, $C_{ss}$ increases by about 15%. However, with the same variation in $C_0$, $C_d$ increases by only about 0.5%. If, on the other hand, a 1000-Å native-oxide insulating layer and a more typical carrier concentration of $2 \times 10^{16}$ $cm^{-3}$ were used, one would have $C_0 \sim C_d$. The result of this would be to compress the maximum variation in $C_s$ by more than an order of magnitude, thus greatly decreasing the resolution of the measurement.

Our measured values of $C_s$ and D for Si-58 are plotted in Fig. 9. In this case a slightly more complicated equivalent circuit is needed to explain the experimental data. There is now a substantial inversion-layer capacitance $C_i$ and resistance $R_i$ in addition to the usual fast interface-state contribution.[2,9] The presence of both effects is evidenced most clearly from the two well-resolved peaks seen in a $G_p/\omega$ vs. frequency plot,[2,13] where $G_p$ is the total parallel conductance of the semiconductor and interface (excluding the insulating layer) as illustrated in Fig. 10. We have also found it necessary in this case to introduce small circuit-element pairs $C_2$, $R_2$ and $C_3$, $R_3$ in addition to $C_1$, $R_1$ to obtain a good fit to the data.[14] The numerical values of the fitted capacitances and corresponding time constants

$$\tau_{ss} = R_{ss} C_{ss} \quad , \tag{21}$$

etc., are given in Table IV. Note that, in contrast to the GaAs case, only

$$\tau_i = R_i C_i \quad , \tag{22}$$

and neither $C_d$ nor $\tau_{ss}$, vary significantly with light intensity. In this regard, it should be emphasized that the dc and ac light variation of $C_d$ aren't expected to be the same. From Eq. (10) of the simple theory developed in Sec. II, for example, one sees that the former depends strongly on the effective recombination time $\tau_\lambda$ while the latter does not.

B. Measured vs. Generated Signal Voltage

The measurement of $C_s$ and D and the determination of the equivalent circuit permits one to precisely relate the measured signal voltage $V_s$ to that generated by the depletion layer, $V_s^0$. The signal voltage is measured by a (PAR model HR-8) lock-in-amplifier with an input impedance of $R_L$ = 10 MΩ and

$V_s$ is the magnitude of the voltage across the load resistor $R_L$. To relate $V_s$ to $V_s^0$ one may use the general equivalent circuit of the device and amplifier shown in Fig. 11a, where Z denotes the total impedance associated with the inversion layer and insulator-semiconductor interface. One may further eliminate any dependence of the result on the particular form of Z by relating it to the measured values of $C_s$ and D for the device:

$$\frac{D}{\omega C_s} + \frac{1}{i\omega C_s} = R_0 + \frac{1}{i\omega C_0} + \frac{1}{\frac{1}{Z} + i\omega C_d} \quad . \tag{23}$$

Using this result and Fig. 11a, one obtains exactly

$$V_s = \omega R_L C_d \left[ \frac{\left(1 - \frac{C_s}{C_0}\right)^2 + \left(D - \omega R_0 C_s\right)^2}{1 + \left(D + \omega R_L C_s\right)^2} \right]^{1/2} V_s^0 \quad . \tag{24}$$

In the GaAs samples, $C_s$ is always sufficiently large and $R_0$ sufficiently small for the chopping frequencies employed that

$$\omega R_L C_s \gg 1 > D \gg \omega R_0 C_s \quad . \tag{25}$$

In this limit, Eq. (24) simplifies to

$$\begin{aligned} V_s &= \frac{C_d}{C_s}\left[\left(1 - \frac{C_s}{C_0}\right)^2 + D^2\right]^{1/2} V_s^0 \\ &\cong \frac{C_d}{C_s} V_s^0 \quad . \end{aligned} \tag{26}$$

This result almost completely reconciles the measured responsivity $R_\lambda^*$ with the simple theory developed in Sec. II for the generated responsivity $R_\lambda^{*,0}$. At either low light intensity or high frequency $C_s \sim C_d$, as can be seen from Fig. 8, and little difference between $R_\lambda^*$ and $R_\lambda^{*,0}$ is expected. At high intensity and low frequency, however, $C_s \gg C_d$ due to the large contribution of the interface states, and hence $R_\lambda^* \ll R_\lambda^{*,0}$. This explains the behavior noted in Fig. 5,

for example. If one now plots instead the apparent generated responsivity $R_\lambda^{*,0}$ versus frequency, using Eq. (24), then the expected $\omega^{-1}$ behavior is seen in all cases, as shown in Fig. 12.

In Si-58, on the other hand, $C_s$ is generally an order of magnitude smaller than in the GaAs samples due to the much larger active area of the latter. This results in considerable loading of the measured signal by $R_L$ in the Si case, as already noted in Sec. II. When $R_\lambda^{*,0}$ is extracted from $R_\lambda^*$ via Eq. (24), the agreement with the simple theory is comparable to that obtained for the GaAs samples. At low light intensity ($10^{-3}$ filter), $\lambda = 0.82$ μm, and $f = 13$ Hz, for example, we infer experimental values for $R_\lambda^{*,0}$ of 6.1, 2.0 and 2.1 x $10^5$V-cm$^2$/W for Si-58, GaAs-7 and GaAs-10, respectively. These values are all approximately 50% of the ideal upper limits quoted in Sec. II. We further infer from Eq. (13) respective quantum efficiencies $\eta_\lambda$ of 0.53, 0.47 and 0.44. These are quite reasonable values and their approximate constancy is very supportive of the theoretical interpretation of our results.

C. Noise

Determination of the equivalent circuit also permits one to predict the noise voltage inherent in the device. Unlike the relationship between the measured and generated signal voltages, however, the result will depend on the details of the impedance Z associated with the interface states and inversion layer. If Z consists of a parallel network of capacitor, resistor pairs as we have assumed above, then the noise voltage $V_n^{(k)}$ across $R_L$ due to the $k^{th}$ pair may be calculated from the equivalent circuit shown in Fig. 11b. The result is

$$V_n^{(k)} = \omega R_L C_k \left[ \frac{\left(1 - \frac{C_s}{C_o}\right)^2 + \left(D - \omega R_o C_s\right)^2}{\left(1 + \omega^2 \tau_k^2\right)\left(1 + \left(D + \omega R_L C_s\right)^2\right)} \right]^{1/2} V_{nk} \quad , \tag{27}$$

where $V_{nk}$ is the Johnson or thermal noise associated with the resistor $R_k$,

$$V_{nk} = \left(4kT R_k \Delta f\right)^{1/2} \quad . \tag{28}$$

Since the noise sources have random phases, one may calculate the total noise voltage $V_n$ as the rms average of the individual $V_n^{(k)}$:

$$\begin{aligned} V_n &= \left( \sum_k \left[ V_n^{(k)} \right]^2 \right)^{1/2} \\ &= \omega R_L \left( 4kT \Delta f \sum_k \frac{C_k \tau_k}{1 + \omega^2 \tau_k^2} \left[ \frac{\left(1 - \frac{C_s}{C_o}\right)^2 + \left(D - \omega R_o C_s\right)^2}{1 + \left(D + \omega R_L C_s\right)^2} \right] \right)^{1/2} \end{aligned} \tag{29}$$

In obtaining Eq. (29) only the total negligible contribution due to the sheet resistance $R_0$ has been omitted from the sum.

For the GaAs samples considerable simplification of the general expression (29) is possible. One may again use the inequalities contained in Eq. (25) and also the fact that the noise contribution due to the $C_{ss}$, $R_{ss}$ pair dominates that due to the $C_1$, $R_1$ pair for the GaAs circuit shown in Fig. 8. Furthermore, $\omega\tau_{ss} >> 1$ in the region of interest, so that

$$V_n \cong \frac{1}{\omega R_{ss} C_s} \left(4kT R_{ss} \Delta f\right)^{1/2} \quad . \tag{30}$$

The $\omega^{-1}$ dependence in Eq. (30) is characteristic of surface-state dominated noise in MIS structures.[2] It results from the shunting of the Johnson noise of $R_{ss}$ by the capacitive impedance $(\omega C_d)^{-1}$ of the depletion layer. Equation (30) with $C_s = C_d$ is compared with the directly measured (dark) noise for GaAs-10 in Fig. 13, where the frequency dependence of the noise was measured on the

lock-in-amplifier.[15] The anticipated and measured noise show good qualitative agreement, but the former is about a factor of 3 too large. We attribute this to inaccuracies in determining the purely resistive elements in the impedance Z. In this regard, we note that the impedance of a surface-state continuum, unlike that of a single level, is only accurately represented as a series capacitor, resistor pair for $\omega\tau_{ss} << 1$.[9,14]

The frequency dependence of the noise in Si-58 shows a somewhat more complicated behavior due to contributions from both the interface and the inversion layer. The full expression (29), used in combination with the Si equivalent circuit shown in Fig. 9, gives the correct qualitative behavior but is again quantitatively too large with respect to the directly measured noise, as shown in Fig. 14. The largest different between the theoretical and experimental results here occurs in the high frequency region where the noise is dominated by the interface states. This reinforces our suspicions about modeling the interface-state impedance in terms of series capacitor, resistor pairs.[14]

D. Optimization of $D_\lambda^*$

Although Eq. (29) for $V_n$ is of limited quantitative accuracy, it is informative to combine this result with Eqs. (2), (13) and (24) to obtain the expected detectivity of a photocapacitive MIS device:

$$D_\lambda^* = \frac{e\eta_\lambda}{E_\lambda}\left[4kT\sum_k \frac{(C_k/A)\,\tau_k\,\omega^2}{1+\omega^2\tau_k^2}\right]^{-1/2} . \tag{31}$$

Both the depletion-layer capacitance $C_d$ and the load resistance $R_L$ have cancelled out of this result. The ultimate factors limiting $D_\lambda^*$ become the capacitances $C_k$ and time constants $\tau_k$ associated with the inversion layer and

interface. In the GaAs samples, Eq. (31) may be simplified in the same manner as above to yield

$$D_\lambda^* \cong \frac{e\eta_\lambda}{E_\lambda}\left(\frac{\tau_{ss} A}{4kTC_{ss}}\right)^{1/2} , \tag{32}$$

which is independent of frequency. The interface-state capacitance $C_{ss}$ is determined by the density of interface states $N_{ss}$,[2,9]

$$C_{ss} = eAN_{ss} , \tag{33}$$

while the corresponding time constant depends on the capture cross section $\sigma_{ss}$ and density of electrons at the interface according to[2,9]

$$\tau_{ss} = \frac{\exp(-e\psi_s/kT)}{\sigma_{ss} V_{th} n_b} , \tag{34}$$

where $v_{th}$ is the thermal velocity of the electrons. Substituting Eqs. (33) and (34) in Eq. (32) exposes the dependence of $D_\lambda^*$ on the material parameters which may be controlled:

$$D_\lambda^* = \frac{e\eta_\lambda}{E_\lambda} \frac{\exp(-e\psi_s/2kT)}{(4kT\sigma_{ss} V_{th} n_b e N_{ss})^{1/2}} . \tag{35}$$

Interestingly, the premium on a low carrier concentration and a large negative surface potential found for the responsivity $R_\lambda^{*,0}$ has returned. There is also a clear reward for an interface with surface states of low density and a small capture cross section. In this regard, the measured values of $N_{ss}$ and $\sigma_{ss}$ for our GaAs samples ($N_{ss} \sim 10^{12} v^{-1} cm^{-2}$ and $\sigma_{ss} \sim 10^{-5}$-$10^{-9} cm^2$) are both very large with respect to the current standards of excellence for insulator-semiconductor interfaces.[9]

The case of Si, on the other hand, is again somewhat more complicated. At sufficiently high frequency ($\sim 10^3$-$10^4$Hz in Si-58), the detectivity will be surface-state limited and the above considerations apply. However, the high frequency $D_\lambda^*$ can be much less than that at low frequency, even in the weak inversion regime. In Si-58, for example, we find $D_\lambda^*$ at 2000Hz a factor of 6 less than that at 13 Hz. Presumably, the low frequency $D_\lambda^*$ in Si devices could be increased by lowering the surface potential $\psi_s$ to near midgap so that no inversion layer is formed. However, this can only be advantageously done to the extent that $\tau_{ss}$ does not become so short that the noise is amplifier limited. In this regard, a low carrier concentration $n_b$ is again beneficial.

## IV. CONCLUSIONS

We have demonstrated that narrow-band, high-detectivity infrared sensors can be produced by using MIS structures in a photocapacitive mode. Even without the optimization of material parameters, room-temperature peak detectivities on the order of $10^{13}$cm-Hz$^{1/2}$/W at 13 Hz have been consistently achieved in Si and GaAs devices with $LaF_3$ or composite $LaF_3$/native oxide insulating layers. This performance exceeds that of conventional solid-state detectors, including photoconductors and p-i-n photodiodes. Our fundamental studies on MIS structures further suggest that comparatively high detectivities can be expected in a wide range of semiconducting materials and hence over the entire infrared spectral range. In particular, it should be possible to use cooled narrow-band semiconductors such as InSb and $Hg_xCd_{1-x}Te$ to advantage in the long-wavelength regime.

Our studies have also isolated the most important material parameters affecting the responsivity and detectivity of photocapacitive MIS systems. These parameters are primarily the bulk carrier concentration $n_b$, the surface potential $\psi_s$ at the insulator-semiconductor interface and the density $N_{ss}$ and capture cross section $\sigma_{ss}$ of interface states. Present indications are that the quantities $n_b$, $N_{ss}$ and $\sigma_{ss}$ should be generally minimized, while the magnitude of $\psi_s$ should be maximized subject to the constraints of no external bias and no inversion-layer formation. However, aside from our deliberate use of low-carrier-concentration semiconducting material, no attempt has yet been made to determine the practical limit

to which these parameters can be advantageously varied. It seems likely, therefore, that even higher values of $R_\lambda^*$ and $D_\lambda^*$ will be forthcoming in optimally-engineered detectors.

The ultimate technological usefulness of our devices for infrared-sensor applications, of course, will depend on many factors in addition to the detectivity and the range of spectral response. These include chemical stability, response time, susceptibility to microphonics, ease of fabricating arrays, and compatibility with integrated optics and processing circuitry. It is already clear that many properties of our devices meet special application requirements quite well. For example, the spectral response of the Si detectors peaks near the emission wavelength of GaAs lasers. Also, preliminary measurements have shown that even our unoptimized Si devices out-perform state-of-the-art p-i-n photodiodes up to 1 MHz. We anticipate that this can be extended up to 20 MHz and possibly beyond with suitably-designed detectors. These devices may consequently find applications in optical communications and computing systems. Finally, array fabrication of these MIS structures using standard photolithography methods should be relatively simple.

## ACKNOWLEDGMENTS

This work was supported in part by NASA grant NSG-1385. We wish to thank W. R. Feltner who grew the $SiO_2$ layers, T. C. Steele for help with sample preparation, and E. J. Chern, B. A. Seiber, and P. Su for assistance with the experiments.

REFERENCES

1. A. Sher, R. K. Crouch, S. S.-M. Lu, W. E. Miller and J. A. Moriarty, Appl. Phys. Lett. 32, 713 (1978).

2. The physics of MIS devices is reviewed by S. M. Sze, Physics of Semiconductor Devices (Wiley, New York, 1969), pp. 425-504.

3. H. Levinstein, in Semiconductors and Semimetals, edited by R. K. Willardson, and A. C. Beer (Academic, New York, 1970), Vol. 5, p. 10.

4. A. Sher, W. E. Miller, Y. H. Tsuo, J. A. Moriarty, R. K. Crouch, and B. A. Seiber, Appl. Phys. Lett. (in press).

5. The maximum $D_\lambda^*$ we have measured to date has been $4 \times 10^{13} W^{-1} cmHz^{1/2}$.

6. The responsivity is often defined as $R_\lambda = V_s/(P_o A)$. Since our measured signal voltage $V_s$ is independent of the area A, we find $R_\lambda^* = AR_\lambda$ a more useful characterization of device response.

7. P. W. Kruse, L. D. McGlauchlin and R. B. McQuistan, Elements of Infrared Technology, (Wiley, New York, 1963), p. 122.

8. The surface potential $\psi_s$, carrier concentration $n_b$, and depletion-layer capacitance $C_d$ were determined by standard capacitance-measurement techniques discussed in Refs. 2 and 9.

9. A. Geotzberger, E. Klansmann and M. J. Schulz, CRC Critical Reviews in Solid State Sci. 6, 1 (1976).

10. R. S. Nakhmanson, Solid-State Electron. 18, 617 (1975).

11. All data were obtained with a GR 1620 capacitance measuring assembly. The measured values of $C_s$ and D were found to be independent of the wavelength of the incident light as long as the absorption depth of

the semiconductor remains within an order of magnitude of the depletion-layer thickness. The data presented here and in Ref. 4 refers to $\lambda = 0.82$ μm.

12. The notation in Ref. 4 differs slightly from that used here. In Ref. 4 $C_i \equiv C_{ss}$, $R_i \equiv R_{ss}$ and $\tau_i \equiv \tau_{ss}$.

13. E. H. Nicollian and A. Goetzberger, Bell Sys. Tech. Jour. 6, 1055 (1967).

14. We have recently discovered that if the impedance of the interface states is represented by the functional form appropriate to a continuum of surface states (Eq. (10) of Ref. 9) instead of the series combination of $C_{ss}$ and $R_{ss}$, the Si-58 data can be fit without the three extra circuit-element pairs. This primarily affects the interpretation of $\tau_{ss}$ and $R_{ss}$. Using a continuum model in Si-58, for example, one would conclude that $\tau_{ss}$ is about a factor of 2 larger than the value found with the equivalent circuit shown in Fig. 9.

15. To measure the noise, the output of the PAR lock-in-amplifier was rectified and integrated for times (3-4 min.) long compared to the period associated with the bandwidth setting of the PAR (usually 0.53 Hz). A calibrated noise source was used to determine the transfer characteristic of the entire system.

TABLE I. Relevant physical parameters of the three MIS samples discussed in the text: total device thickness L(μm); active area A($cm^2$), insulator capacitance $C_0$(nF), bulk carrier concentration $n_b$($cm^{-3}$), surface potential $\psi_s$(V), depletion-layer capacitance $C_d$(nF), and the 13 Hz maximum responsivity $R^*_{\lambda,max}$($10^5$V-$cm^2$/W), maximum detectivity $D^*_{\lambda,max}$($10^{13}W^{-1}cmHz^{1/2}$), and measured noise voltage $V_n$(μV).

| Sample | Insulator | L | A | $C_0$ |
|---|---|---|---|---|
| Si-58 | 250Å $LaF_3$/250Å $SiO_2$ | 300 | 0.042 | 5.13 |
| GaAs-7 | 250Å $LaF_3$ | 25[a] | 0.3 | 320 |
| GaAs-10 | 500Å $LaF_3$/250Å native oxide | 25[a] | 0.3 | 85.0 |

| | $n_b$ | $-\psi_s$ | $C_d$ | $R^*_{\lambda,max}$ | $D^*_{\lambda,max}$ | $V_n$ |
|---|---|---|---|---|---|---|
| Si-58 | $2.4 \times 10^{14}$ | 0.44 | 0.297 | 1.14 | 0.51 | 0.080 |
| GaAs-7 | $3.1 \times 10^{15}$ | 0.85 | 5.57 | 1.98 | 1.20 | 0.022 |
| GaAs-10 | $3.1 \times 10^{15}$ | 1.05 | 5.02 | 1.75 | 0.78 | 0.030 |

[a]Epitaxial layer grown on degenerate substrate.

TABLE II. Average photon flux $\Phi$ (number/cm$^2$-sec) and power density $P_0$(W/cm$^2$) at $\lambda$ = 0.82 μm for the neutral-density filters used in the present experiments.

| Filter | $\Phi$ | $P_0$ |
|---|---|---|
| $10^0$ (no filter) | $4.38 \times 10^{12}$ | $1.06 \times 10^{-6}$ |
| $10^{-1}$ | $4.30 \times 10^{11}$ | $1.04 \times 10^{-7}$ |
| $10^{-2}$ | $7.15 \times 10^{10}$ | $1.73 \times 10^{-8}$ |
| $10^{-3}$ | $5.66 \times 10^{9}$ | $1.37 \times 10^{-9}$ |

TABLE III. Average current density $J_s$, magnitude of the impedance $|Z|$, and generated signal voltage $V_s^0$ for the three ideal photodetectors depicted in Fig. 7. Here $\bar{g}_\lambda = \eta_\lambda P_0/E_\lambda$.

| | $J_s$ | $\lvert Z \rvert$ | $V_s^0$ |
|---|---|---|---|
| photocapacitor | $e\bar{g}_\lambda$ | $\frac{1}{\omega C_d}$ | $e\bar{g}_\lambda [\frac{A}{\omega C_d} = \frac{-2\psi_s}{\omega n_b \ell_d}]$ |
| photoconductor | $e\bar{g}_\lambda \frac{\mu_e V}{\omega L_0^2}$ | R | $e\bar{g}_\lambda \frac{V}{\omega n_b L_0}$ |
| p-i-n | $e\bar{g}_\lambda$ | $\frac{1}{\omega C_{pin}}$ | $e\bar{g}_\lambda \frac{A}{\omega C_{pin}}$ |

TABLE IV. Equivalent circuit parameters for Si-58, with capacitance in nF and time constants in secs. Photon flux for each filter was $2\Phi$, where $\Phi$ is given in Table II.

| Filter | dark | $10^{-2}$ | $10^{-1}$ | $10^{0}$ |
|---|---|---|---|---|
| $C_i$ | 1.09 | 1.27 | 1.69 | 2.95 |
| $\tau_i$ | 0.037 | 0.035 | 0.018 | 0.00425 |
| $C_0$ | | | 5.13 | |
| $C_d$ | | | 0.297 | |
| $C_{ss}$ | | | 0.251 | |
| $\tau_{ss}$ | | | $6.25 \times 10^{-5}$ | |
| $C_1$ | | | 0.0294 | |
| $\tau_1$ | | | $1.73 \times 10^{-3}$ | |
| $C_2$ | | | 0.020 | |
| $\tau_2$ | | | $3.0 \times 10^{-4}$ | |
| $C_3$ | | | 0.035 | |
| $\tau_3$ | | | $2.0 \times 10^{-5}$ | |

## FIGURE CAPTIONS

Fig. 1. Measured responsivity $R_\lambda^*$ and detectivity $D_\lambda^*$ as a function of incident wavelength $\lambda$ and optical intensity for Si-58 at 13 Hz.

Fig. 2. Measured responsivity $R_\lambda^*$ and detectivity $D_\lambda^*$ as a function of incident wavelength $\lambda$ and optical intensity for GaAs-7 at 13 Hz.

Fig. 3. Measured responsivity $R_\lambda^*$ and detectivity $D_\lambda^*$ as a function of incident wavelength $\lambda$ and optical intensity for GaAs-10 at 13 Hz.

Fig. 4. Responsivity per photon, $R_\lambda^*/E_\lambda$, as a function of incident wavelength $\lambda$ and optical intensity for GaAs-7 at 13 Hz.

Fig. 5. Measured responsivity $R_\lambda^*$ as a function of chopping frequency f and optical intensity at a wavelength $\lambda = 0.82$ μm in GaAs-10.

Fig. 6. Apparent generated signal voltage $V_s^0$ vs $(-\psi_s)^{1/2}$, where $\psi_s$ is the insulator-semiconductor interface potential, in a GaAs MIS device whose physical characteristics approximate those of GaAs-7, with $\lambda = 0.82$ μm, $10^{-3}$ filter, and f = 13 Hz. The straight line represents Eq. (13) with a quantum efficiency $\eta_\lambda = 0.34$.

Fig. 7. Schematic representation of three ideal photodetectors discussed in the text. Each device has a horizontal length $L_0$ and an active area A on which the radiation is incident. Regions marked I, n, p, and i denote insulating material and n-type, p-type and intrinsic semiconducting material, respectively. Shaded areas represent metal contacts.

Fig. 8. (a) Total series capacitance $C_s$ and (b) dissipation factor D as function of frequency f and dc optical flux $2\Phi$ for GaAs-10. The solid lines represent parameterized fits to the experimental points based on the equivalent circuit shown in the inset.

Fig. 9. (a) Total series capacitance $C_s$ and (b) dissipation factor D as a function of frequency f and dc optical flux $2\Phi$ for Si-58. The solid lines represent parameterized fits to the experimental points based on the equivalent circuit shown in the inset.

Fig. 10. Normalized parallel conductance $G_p/\omega$ as a function of frequency f and dc optical flux $2\Phi$ for Si-58. The low frequency peak is interpreted as due to the inversion layer and high frequency peak ($5 \times 10^3$ Hz) as due to interface states. The solid lines represent parameterized fits to the experimental points based on the equivalent circuit shown in Fig. 9.

Fig. 11. General equivalent circuit for (a) relating the measured signal voltage $V_s e^{i\phi}$ to the voltage generated by the MIS device, $V_s^o e^{i\phi^o}$; and (b) relating the $k^{th}$ component of the measured noise voltage $V_n^{(k)}$ to the thermal noise voltage $V_{kn}$ associated with the resistor $R_k$ of the $k^{th}$ leg of total interface-inversion-layer impedance Z.

Fig. 12. Apparent generated responsivity $R_\lambda^{*,0}$ as a function of chopping frequency f and optical intensity at a wavelength $\lambda = 0.82$ μm in GaAs-10.

Fig. 13. Measured noise voltage, sample noise voltage (measured minus amplifier), and theoretically expected sample noise voltage, Eq. (30) with $C_s = C_d$, as a function of chopping frequency f in GaAs-10.

Fig. 14. Measured noise voltage, sample noise voltage (measured minus amplifier), and theoretically expected sample noise voltage, Eq. (29), as a function of chopping frequency f in Si-58.

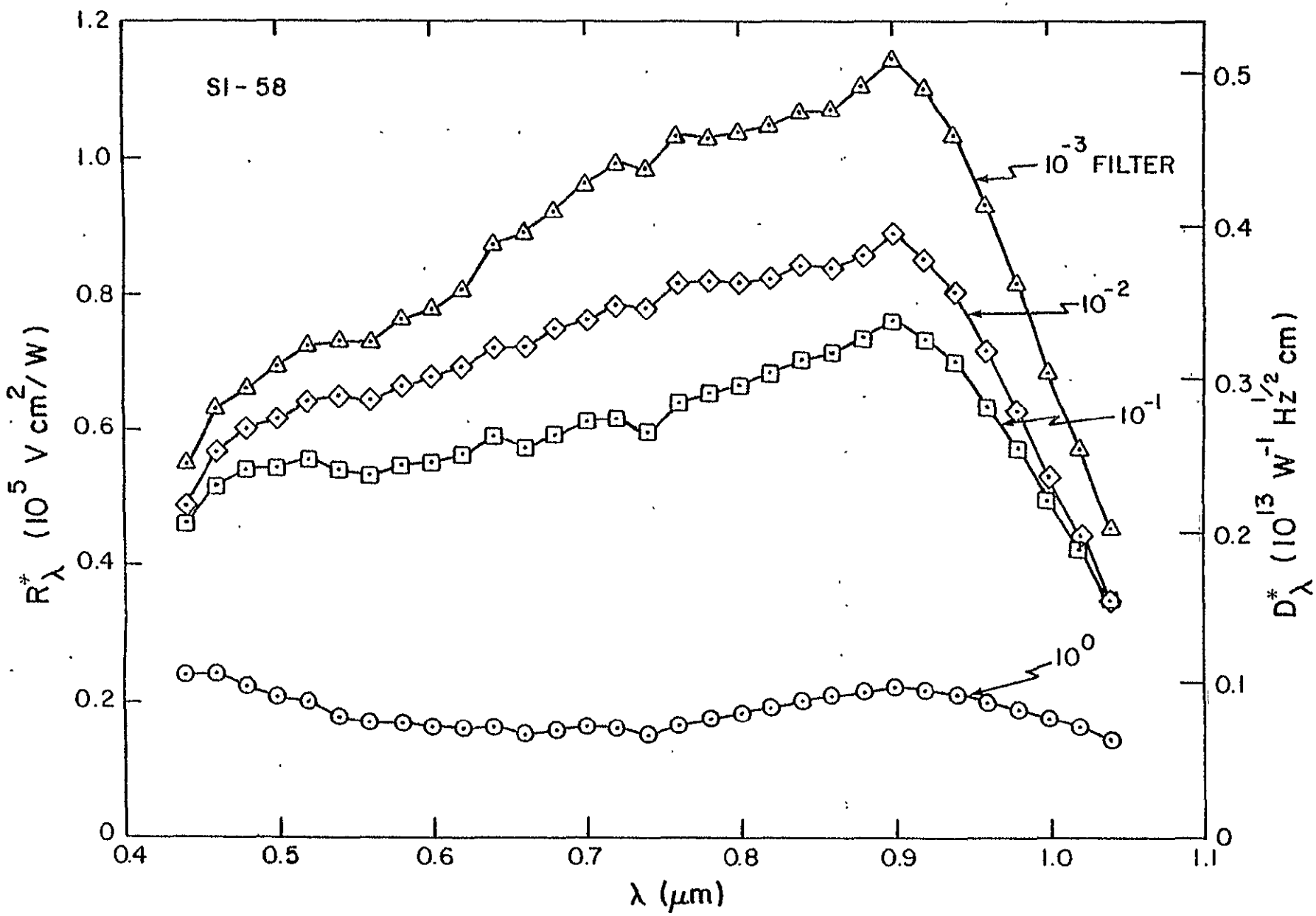
SI - 58
$10^{-3}$ FILTER
$10^{-2}$
$10^{-1}$
$10^{0}$
$R^*_\lambda$ ($10^5$ V cm$^2$/W)
$D^*_\lambda$ ($10^{13}$ W$^{-1}$ Hz$^{1/2}$ cm)
λ (μm)
0
0.2
0.4
0.6
0.8
1.0
1.2
0.1
0.2
0.3
0.4
0.5
0.4
0.5
0.6
0.7
0.8
0.9
1.0
1.1

Fig 1

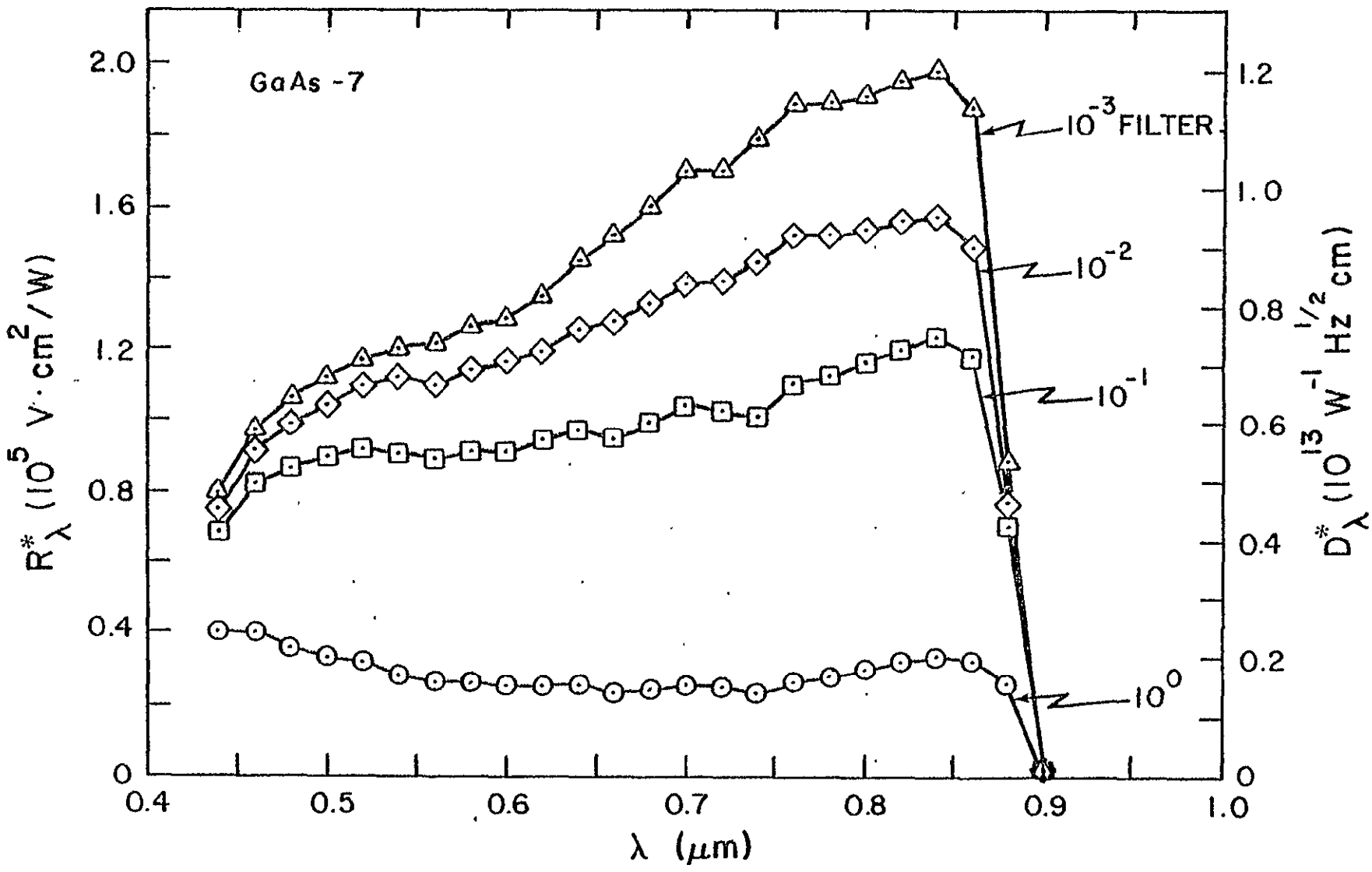
GaAs -7
$10^{-3}$ FILTER
$10^{-2}$
$10^{-1}$
$10^{0}$
$R^*_\lambda$ ($10^5$ V·cm$^2$/W)
$D^*_\lambda$ ($10^{13}$ W$^{-1}$ Hz$^{1/2}$ cm)
λ (μm)
0.4
0.5
0.6
0.7
0.8
0.9
1.0
0
0.4
0.8
1.2
1.6
2.0
0.2
0.6
1.0

Fig. 2

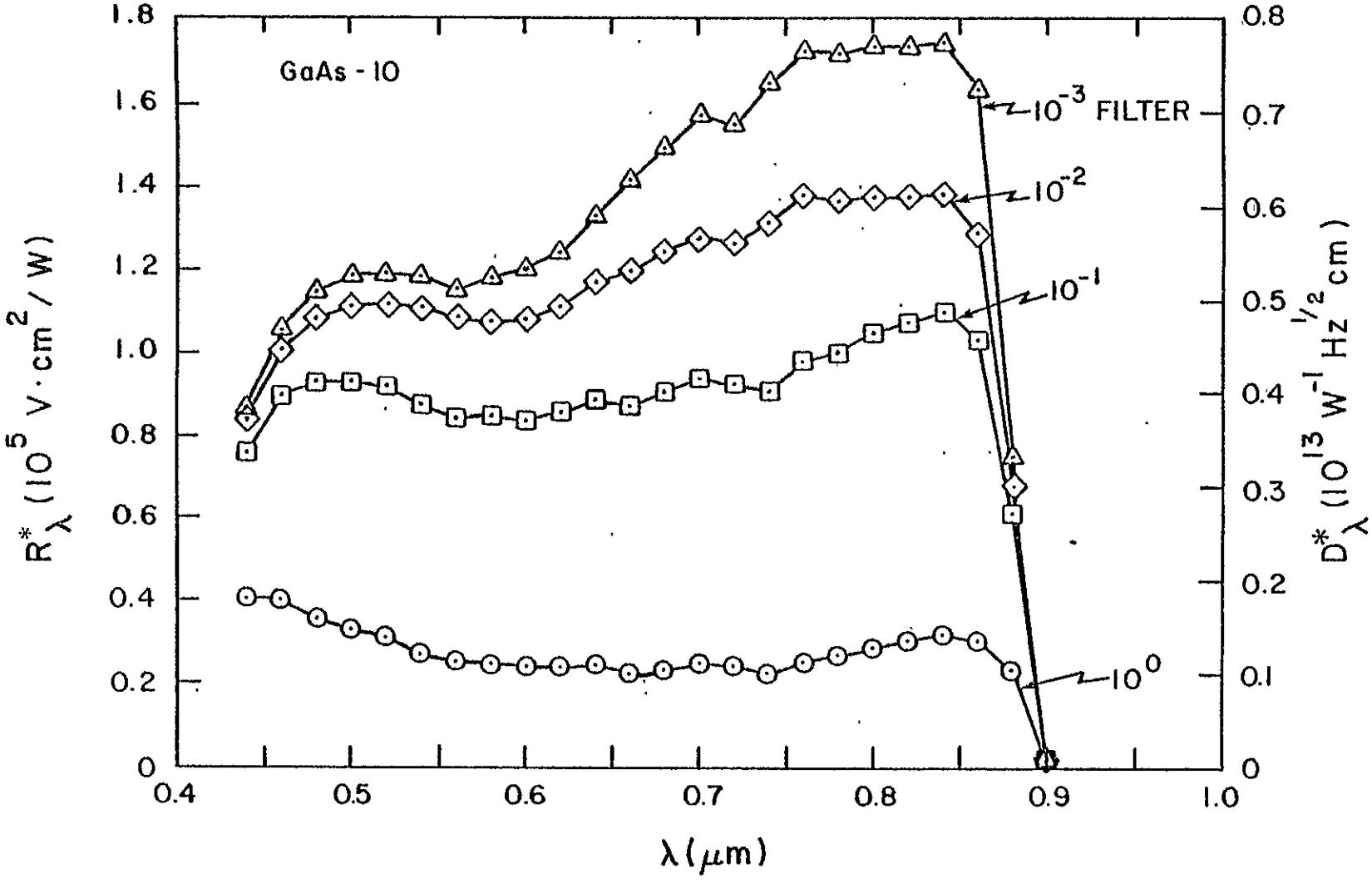
GaAs - 10
$10^{-3}$ FILTER
$10^{-2}$
$10^{-1}$
$10^{0}$
$R^*_\lambda$ ($10^5$ V·cm$^2$/W)
$D^*_\lambda$ ($10^{13}$ W$^{-1}$ Hz$^{1/2}$ cm)
λ (μm)
0
0.2
0.4
0.6
0.8
1.0
1.2
1.4
1.6
1.8
0.1
0.3
0.5
0.7
0.9
0.4
0.5
0.6
0.7
0.8
0.9
1.0

Fig. 3

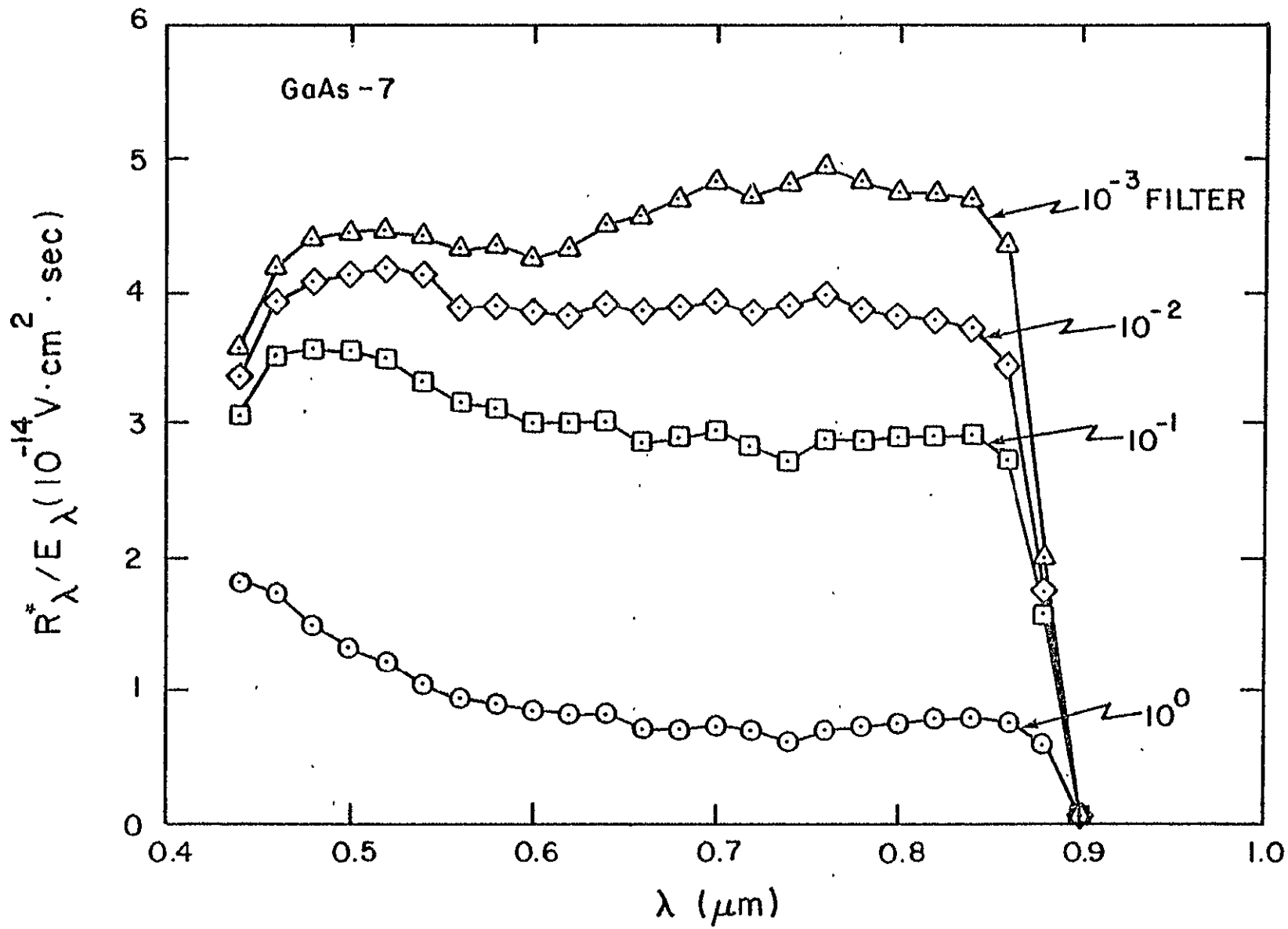
GaAs - 7
$10^{-3}$ FILTER
$10^{-2}$
$10^{-1}$
$10^{0}$
$R^*_\lambda / E_\lambda$ ($10^{-14}$ V·cm$^2$·sec)
λ (μm)
0
1
2
3
4
5
6
0.4
0.5
0.6
0.7
0.8
0.9
1.0

Fig 4.

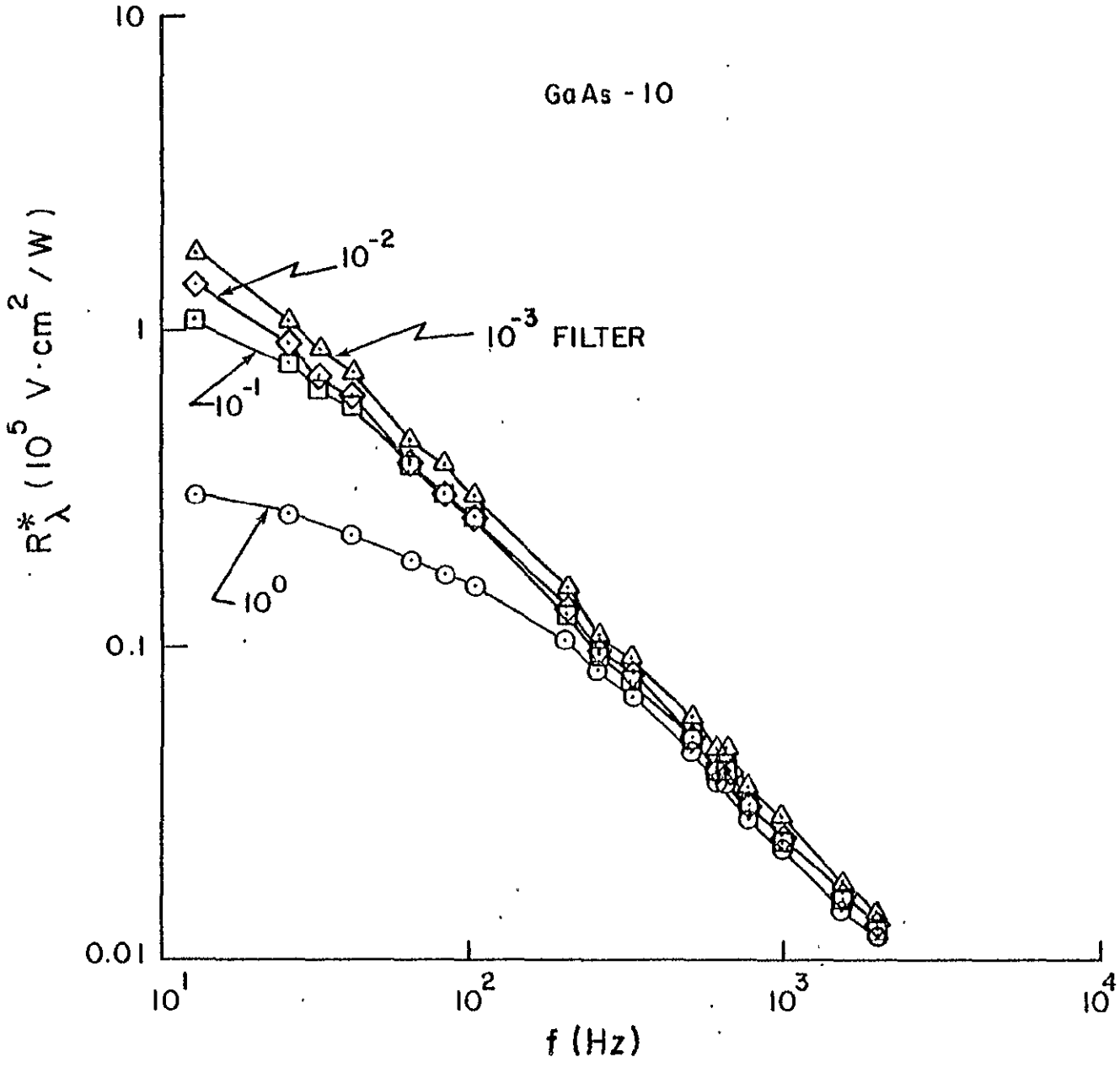
GaAs - 10
$10^{-2}$
$10^{-3}$ FILTER
$10^{-1}$
$10^{0}$
$R^*_\lambda$ ($10^5$ V·cm$^2$/W)
10
1
0.1
0.01
$10^1$
$10^2$
$10^3$
$10^4$
f (Hz)

Fig 5

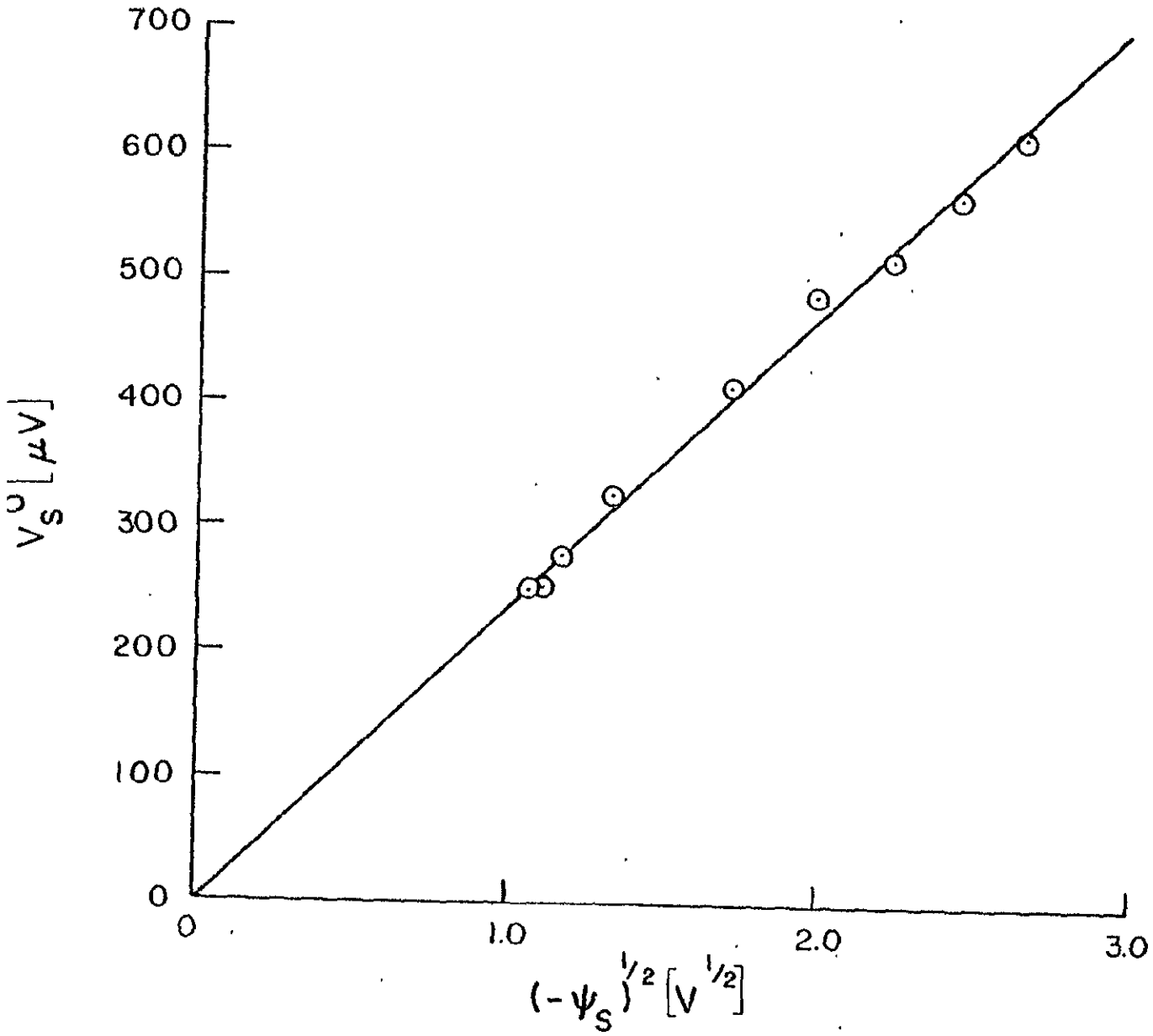


Fig 6

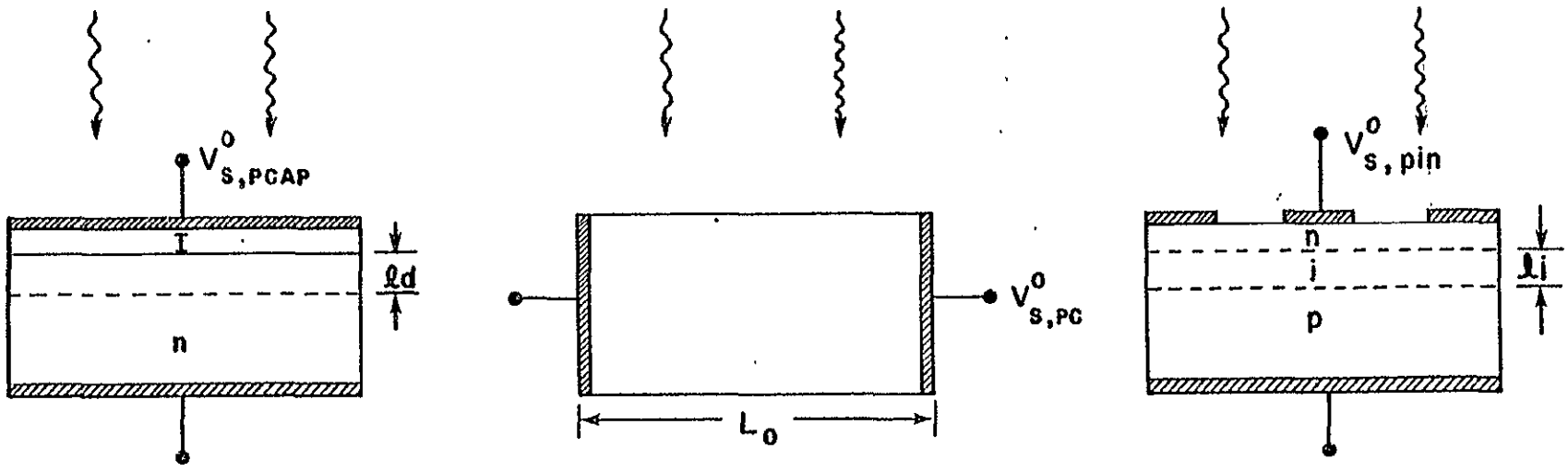


MIS PHOTOCAPACITOR

PHOTOCONDUCTOR

pin DETECTOR

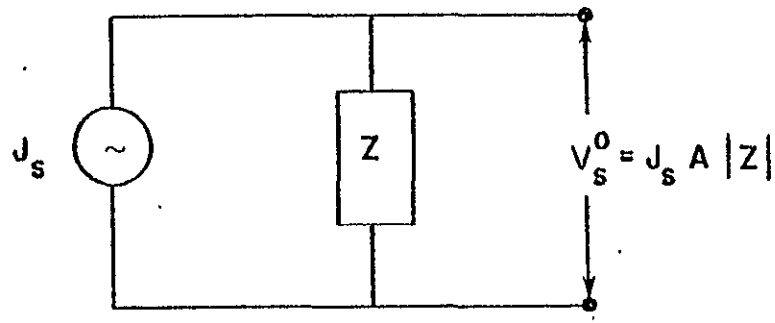


EQUIVALENT CIRCUIT

Fig. 7

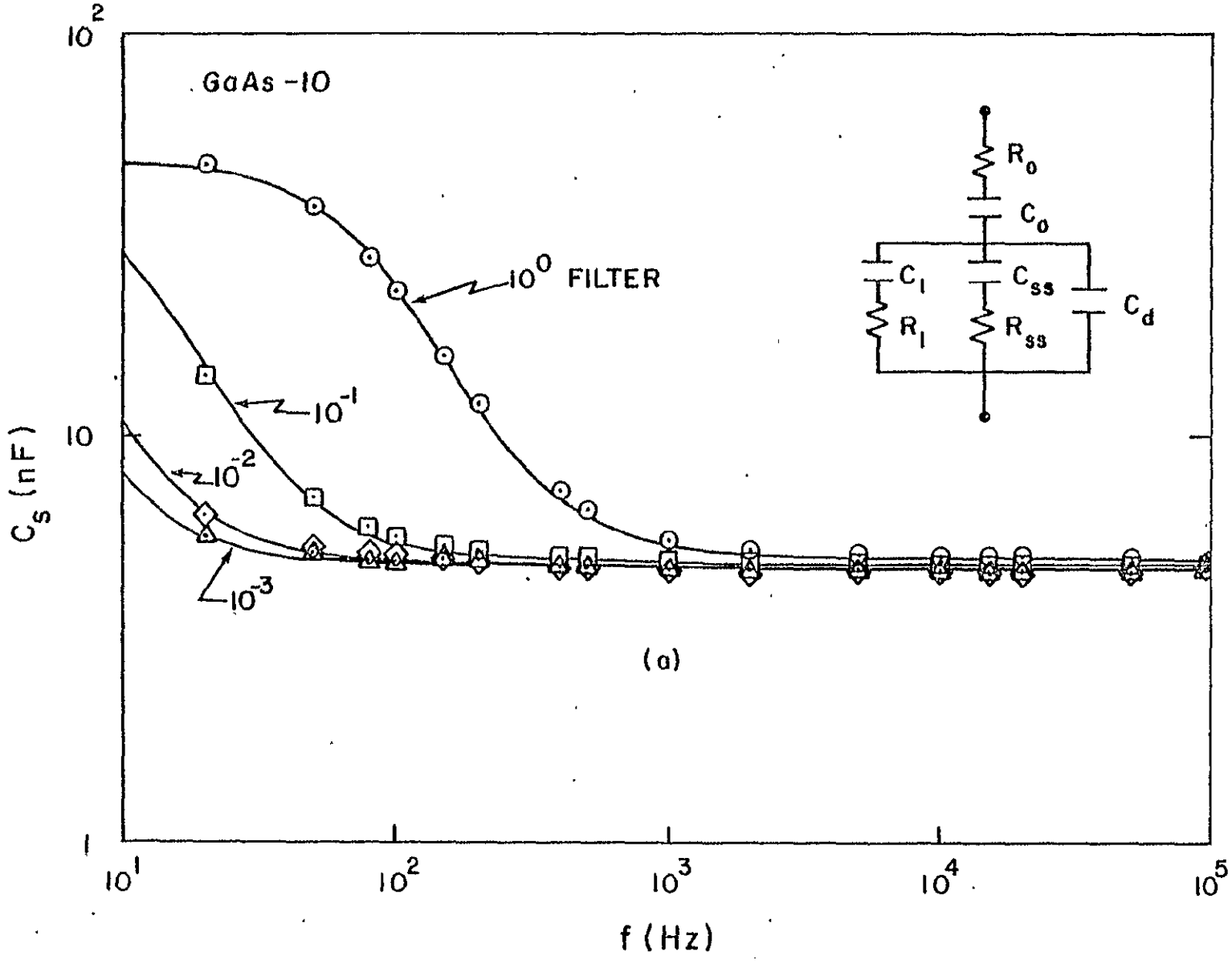
GaAs -10
$10^0$ FILTER
$10^{-1}$
$10^{-2}$
$10^{-3}$
$R_0$
$C_0$
$C_1$
$R_1$
$C_{ss}$
$R_{ss}$
$C_d$
(a)
$C_s$ (nF)
f (Hz)
$10^2$
10
1
$10^1$
$10^2$
$10^3$
$10^4$
$10^5$

Fig 8a

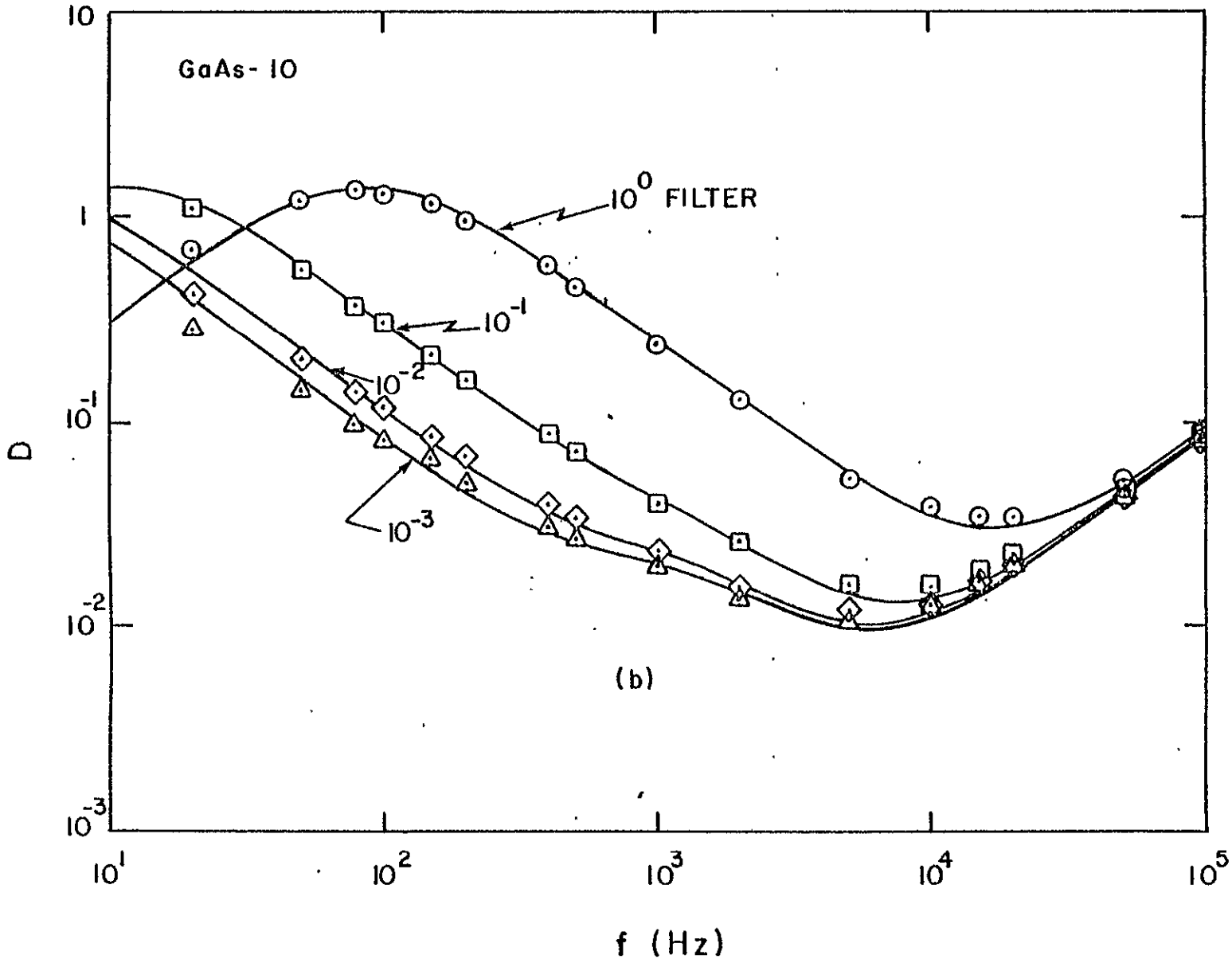
GaAs- 10
$10^0$ FILTER
$10^{-1}$
$10^{-2}$
$10^{-3}$
(b)
D
f (Hz)
10
1
$10^{-1}$
$10^{-2}$
$10^{-3}$
$10^1$
$10^2$
$10^3$
$10^4$
$10^5$

Fig. 8b

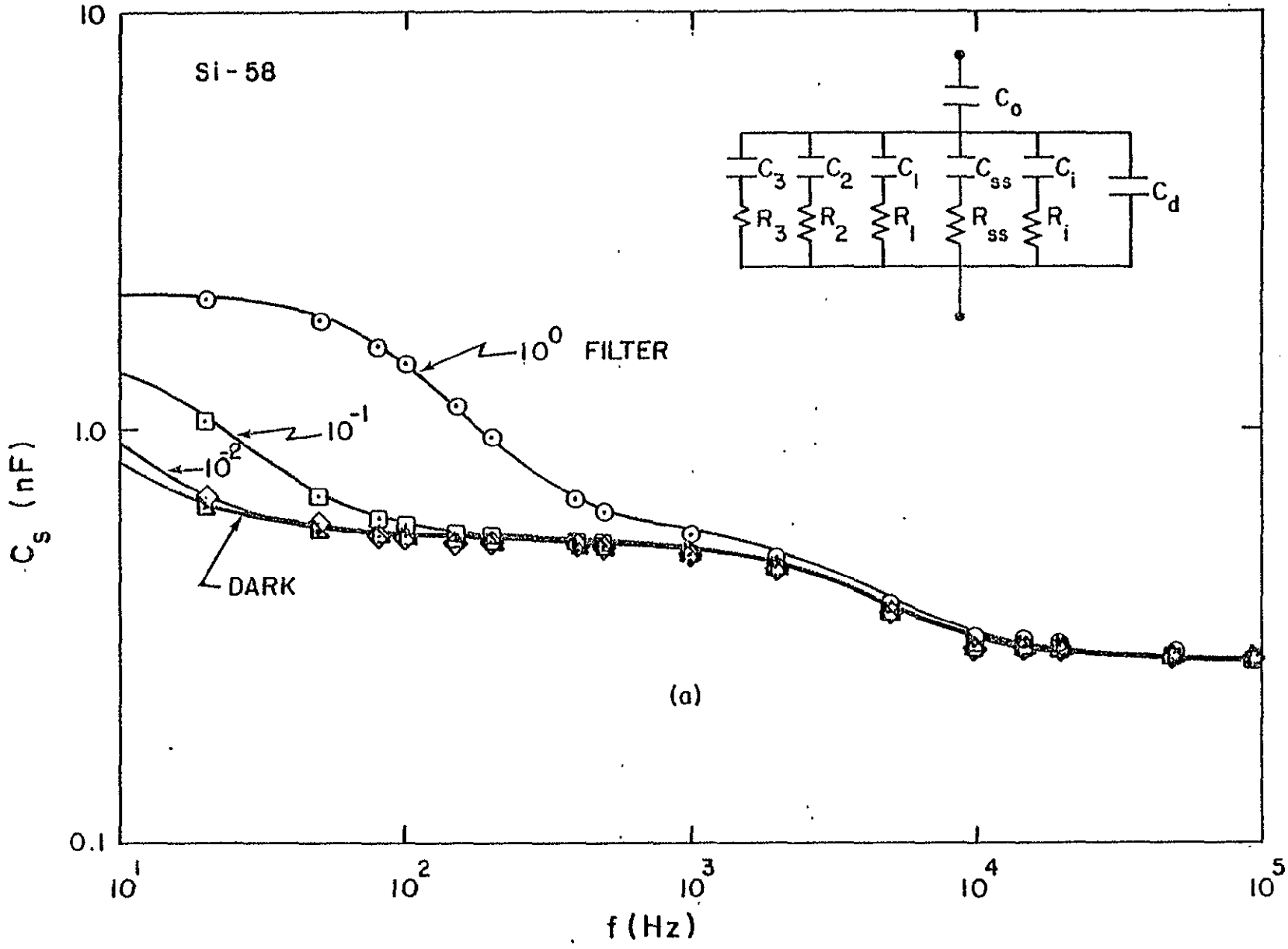
Si - 58
$C_o$
$C_3$
$C_2$
$C_1$
$C_{ss}$
$C_i$
$C_d$
$R_3$
$R_2$
$R_1$
$R_{ss}$
$R_i$
$10^0$ FILTER
$10^{-1}$
$10^{-2}$
DARK
(a)
$C_s$ (nF)
f (Hz)
10
1.0
0.1
$10^1$
$10^2$
$10^3$
$10^4$
$10^5$

Fig 9a

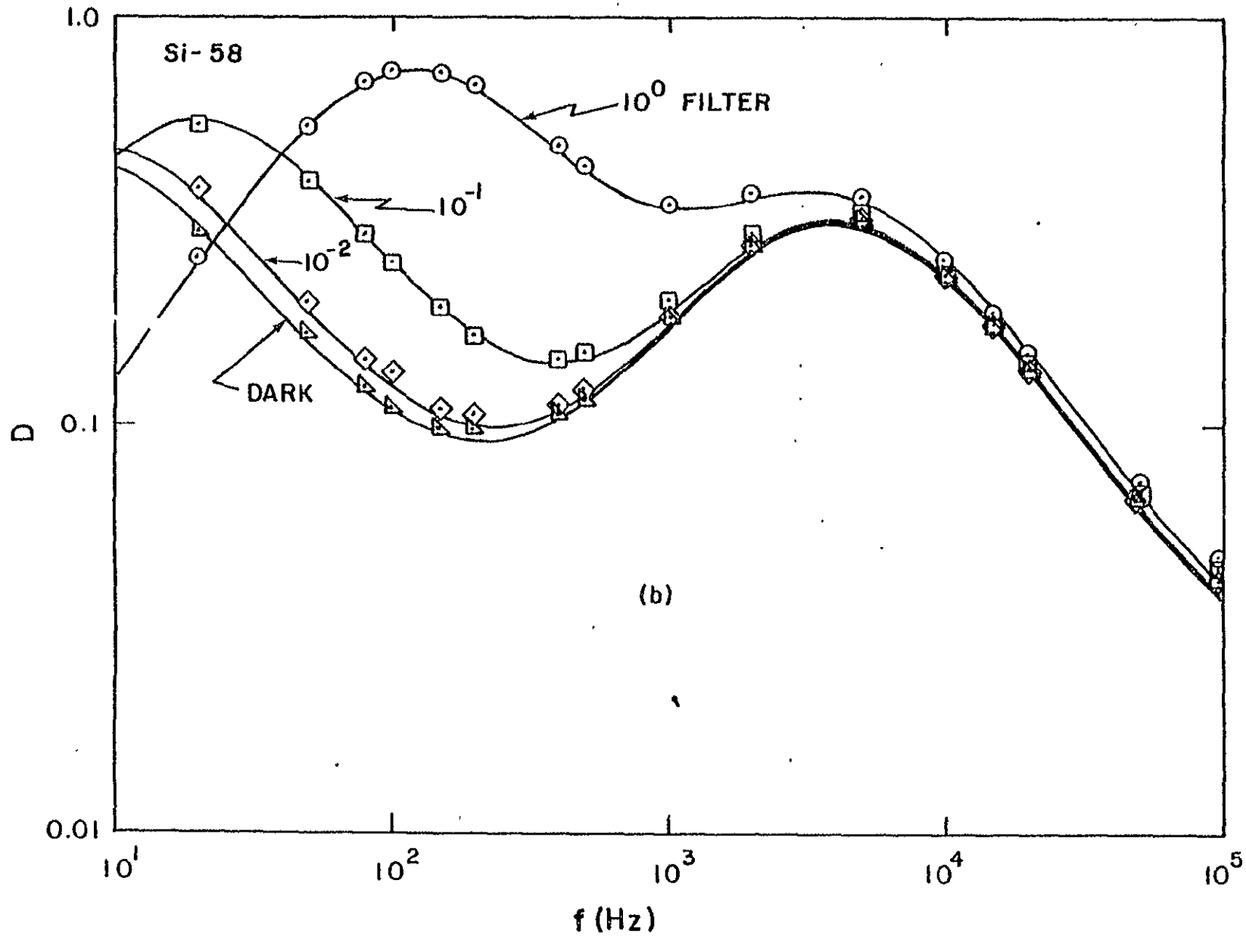
Si-58
$10^0$ FILTER
$10^{-1}$
$10^{-2}$
DARK
(b)
D
1.0
0.1
0.01
$10^1$
$10^2$
$10^3$
$10^4$
$10^5$
f (Hz)

Fig. 9b

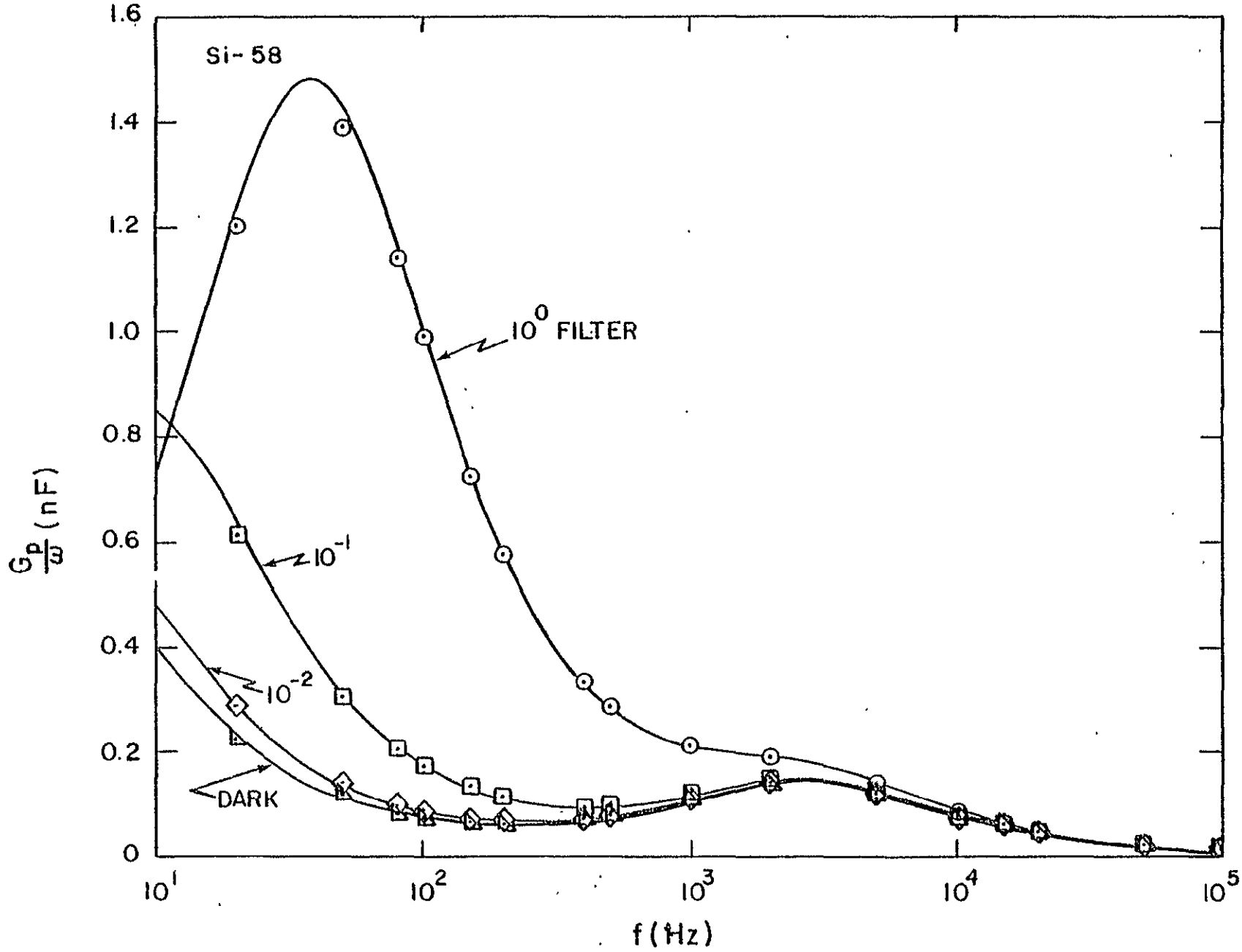
Si-58
1.6
1.4
1.2
1.0
0.8
0.6
0.4
0.2
0
$G^p/B$ (nF)
$10^0$ FILTER
$10^{-1}$
$10^{-2}$
DARK
$10^1$
$10^2$
$10^3$
$10^4$
$10^5$
f (Hz)

Fig 10

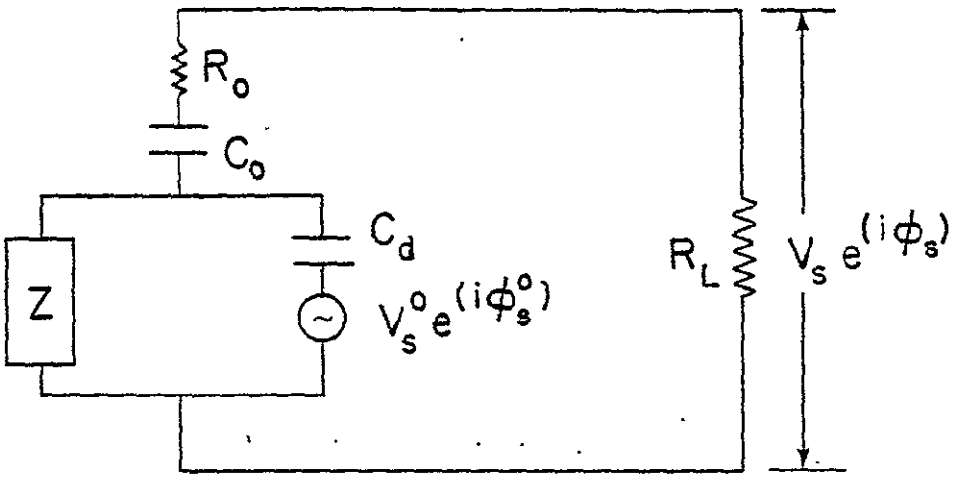


(a)

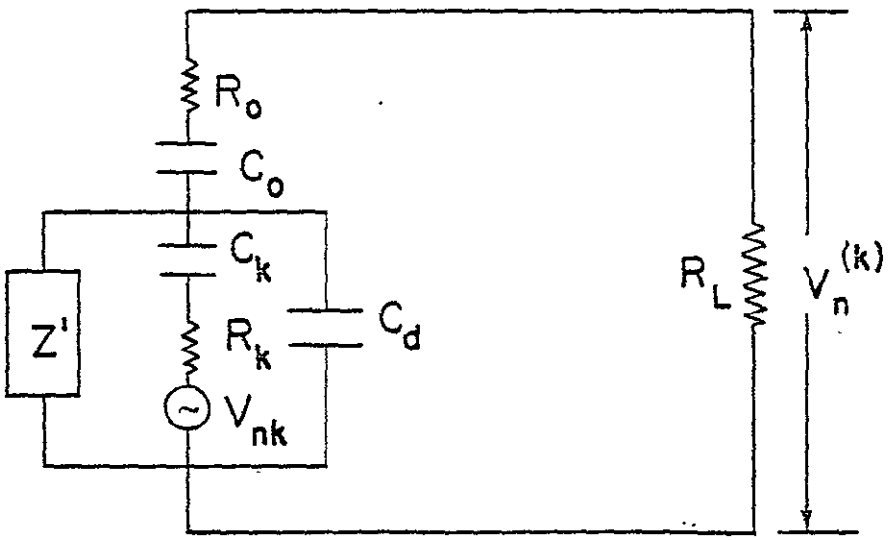


(b)

Fig 11

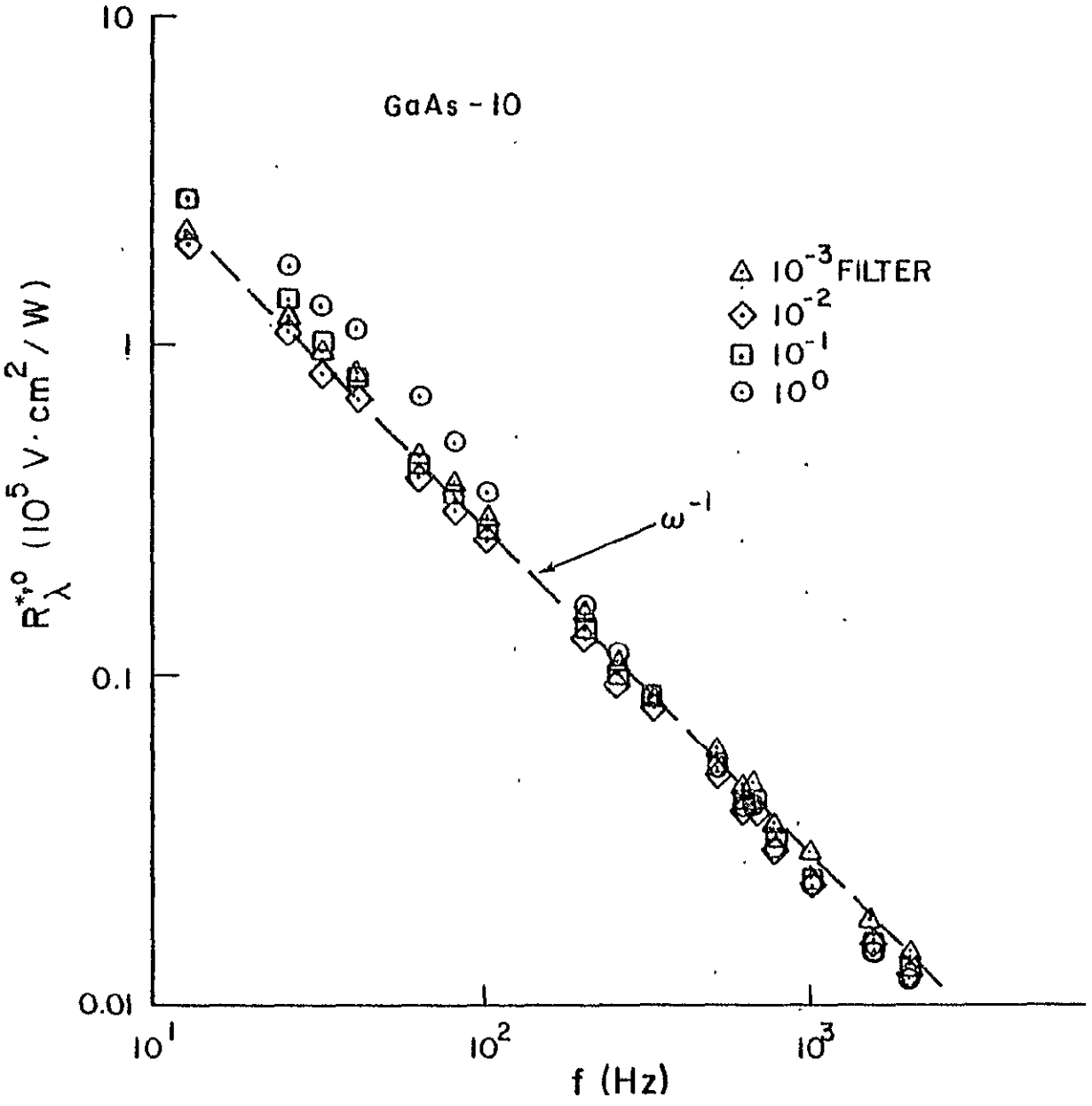
GaAs - 10
10
1
0.1
0.01
$R_\lambda^{*,o}$ ($10^5$ V·cm$^2$/W)
$10^1$
$10^2$
$10^3$
f (Hz)
$\omega^{-1}$
$10^{-3}$ FILTER
$10^{-2}$
$10^{-1}$
$10^0$

Fig.12

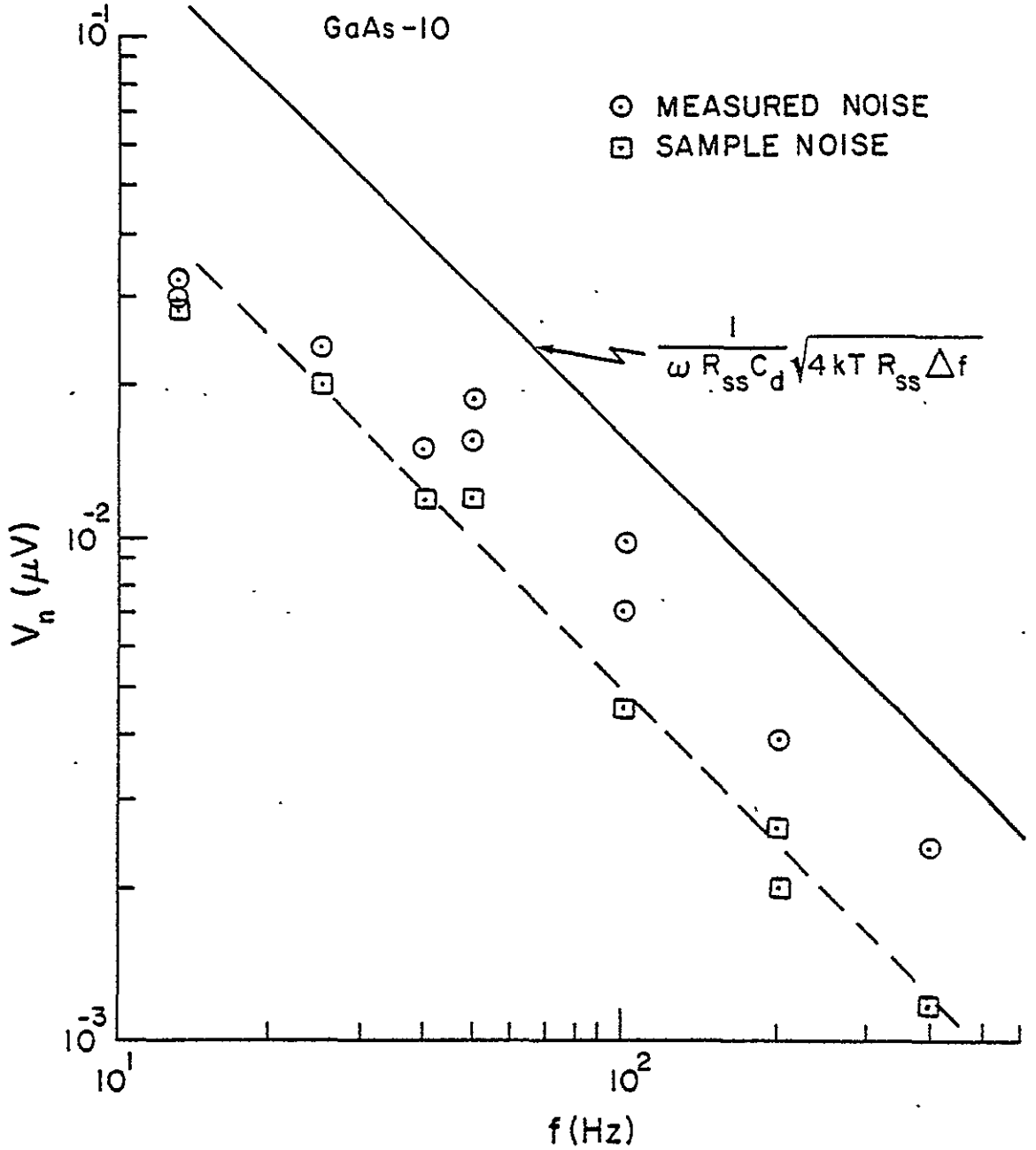
GaAs-10
MEASURED NOISE
SAMPLE NOISE
$\frac{1}{\omega R_{ss} C_d} \sqrt{4kT R_{ss} \Delta f}$
$V_n$ ($\mu$V)
$10^{-1}$
$10^{-2}$
$10^{-3}$
$10^{1}$
$10^{2}$
f (Hz)

Fig 13.

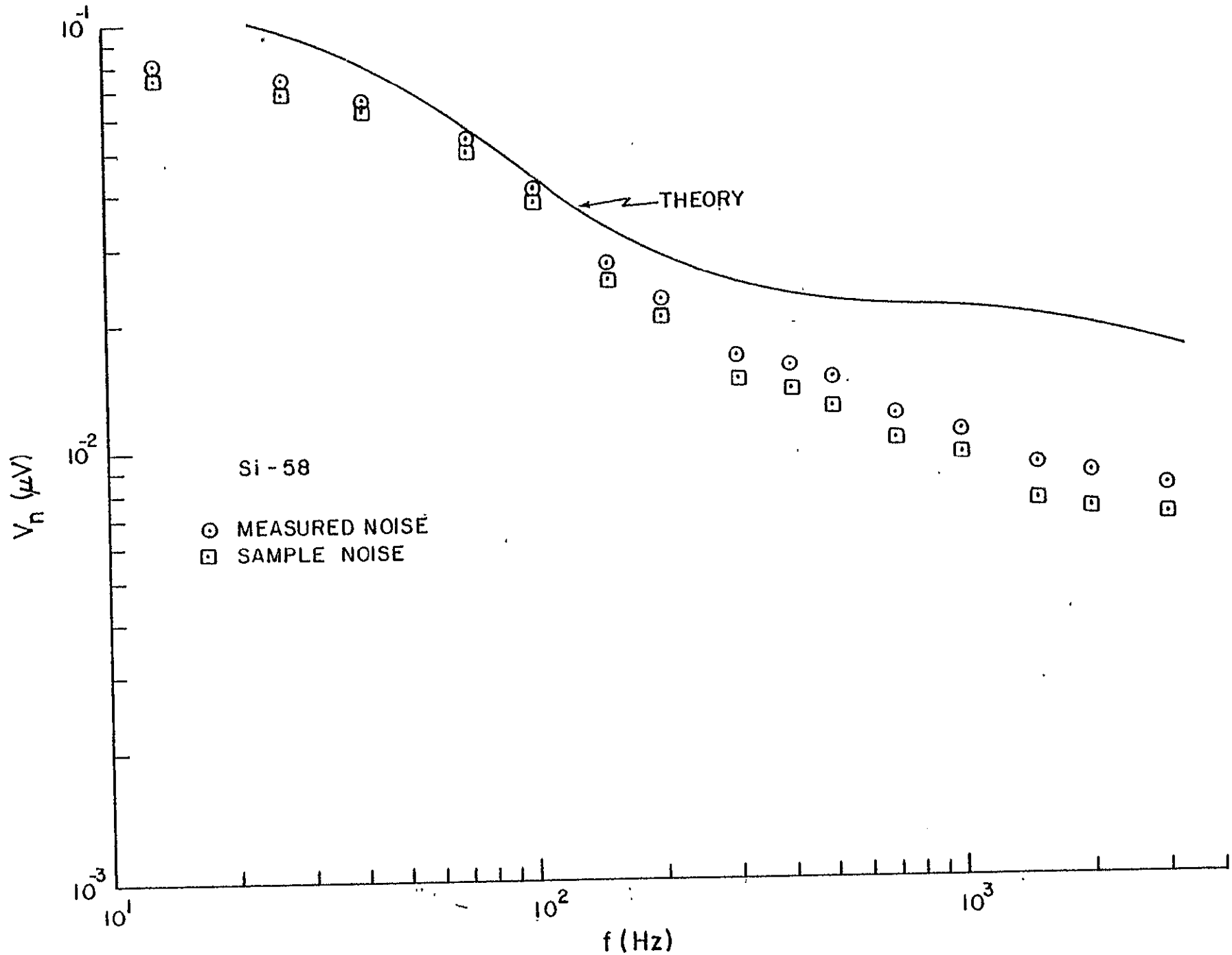
$10^{-1}$
$10^{-2}$
$10^{-3}$
$V_n$ ($\mu$V)
THEORY
Si - 58
MEASURED NOISE
SAMPLE NOISE
$10^1$
$10^2$
$10^3$
f (Hz)

Fig. 14